André Miguel Martins do Nascimento

Licenciatura em Ciências de Engenharia
de Micro e Nanotecnologias

Influence of Degradation on the Charge Transport and Recombination Dynamics of Organic Solar Cells

Dissertação para Obtenção do Grau de Mestre em
Engenharia de Micro e Nanotecnologias

Orientador: Koen Vandewal, Prof. Dr., IAPP-TUD
Co-orientador: Rodrigo Martins, Prof. Dr., FCT-UNL

Júri

Presidente:

Arguentes:

Vogais:

FACULDADE DE
CIÊNCIAS E TECNOLOGIA
UNIVERSIDADE NOVA DE LISBOA

Influence of Degradation on the Charge Transport and Recombination Dynamics of Organic Solar Cells

“I have no doubt that we will be successful in harnessing the sun's energy. ... If sunbeams were weapons of war, we would have had solar energy centuries ago.”

George Porter,

1967 Nobel Prize of Chemistry

Acknowledgements

After a long journey of hard work, another chapter of my life reaches its conclusion. Throughout these years I have lived good and bad moments, exciting adventures and dull classes, I have learned much and forgotten even more. To my institution, the Faculty of Science and Technology of the Nova University of Lisbon, I owe nothing but my gratitude, for it has shaped me into what I am today. This work is dedicated to those who, named or unnamed, have given me their support throughout this journey.

To the Institute of Applied Photophysics, for their warm welcome, and making me feel like one of their own. To Prof. Dr. Karl Leo for accepting me into the Institute. To Prof. Dr. Koen Vandewal for his wise words of guidance and motivation. To Sascha Ullbrich, for unaged measurements of the first run, and for his invaluable advice and help with the equipment, no amount of craft beer or exotic coffee could express my gratitude. To Prof. Dr. Donato Spoltore for unaged measurements of the first run and discussions on transient characterization methods. To Prof. Dr. Christian Körner, for discussions on the Lesker runs and sample reproducibility. To Frederik Nehm, for discussions on degradation. To Sven Kunze, for erasing technical problems. And to Team Bierstube, for all the beer and banter.

To Prof. Dr. Rodrigo Martins, for the opportunities and guidance he gave me, and Prof. Dr. Elvira Fortunato for their share in shaping and promoting our masters degree.

To Justyna Rogińska, her support and patience helped me through the tougher moments of my final stretch.

To Ricardo Relvas, João Patrício, João Cardoso and Samuel Outeiro for all the comraderie, adventures and life discussions. To my good colleagues and friends, Ana Figueiredo, André Lúcio, António Almeida, Beatriz Bruxelas, Bernardo Ferreira, Bruno Fernandes, Carolina Marques, Diogo Lima, Gabriel Souza, Gonçalo Salgado, Jaime Faria and Rodrigo Santos, for all the great work, study and friendships.

To Ana Macedo, Gustavo Galveias, João Branco, Joana Ribeiro, Bruno Magalhães and Funda Aktop, for all the good food, trips and lasting memories.

To my parents, mere words cannot express my gratitude for their unwavering and unconditional support.

Abstract

Organic photovoltaic technology presents itself as a viable and cost-effective renewable energy. However, efficiency must be further increased if its commercialization is to succeed. As such, the main focus of this thesis is on the transport and recombination dynamics of photo-generated charges, which are key for increasing solar cell efficiency. An understanding of the relationship between characteristic device parameters such as fill factor (*FF*), open-circuit voltage (V_{OC}) and short-circuit current (J_{SC}) to material properities such as electron and hole mobilities (μ_n and μ_p), active layer thickness and the bimolecular recombination coefficient (k_2), will be developed. The degradation (85ºC in darkness for 1000h) of organic solar cells, made with proprietary materials from Heliatek GmbH, is studied through the use of basic (current density – voltage (JV) curve, external quantum efficiency (EQE) spectrum) and transient solar cell characterization techniques (Transient photovoltage (TPV), Suns-V_{OC}, open-circuit corrected charge extraction (OTRACE), space charge limited current (SCLC)), performed at the Dresden Integrated Center for Applied Physics and Photonic Materials. Results indicate that the reduction in solar cell efficiency upon aging of the devices is mostly due to a decrease in *FF*, itself caused primarily by a mobility reduction and parasitic resistances. In an attempt to slow down degradation, the addition of a 5nm protective layer is also studied. While this layer decreases the *FF* slightly, a slower degradation of J_{SC} and *FF* outweights this initial loss in *FF*.

Keywords: Organic solar cells, degradation, mobility, transient photovoltage (TPV), open-circuit corrected charge carrier extraction (OTRACE), space charge limited current (SCLC), Suns-V_{OC}

Resumo

A tecnologia fotovoltaica orgânica, apresenta-se como uma energia renovável de custo-efetivo e viável. Contudo, a eficiência terá de ser aumentada para garantir o sucesso da sua comercialização. Como tal, o foco principal desta tese é na dinâmica de transporte e recombinação de cargas foto-geradas, a qual é chave para o aumento da eficiência de células solares. Uma compreensão da relação entre parâmetros característicos do dispositivo como o fill factor (*FF*), tensão de circuito aberto (V_{OC}) e corrente de curto-circuito (J_{SC}) e propriedades dos materiais, como mobilidades de electrão e de buraco (μ_n e μ_p), espessura da camada ativa e o coeficiente de recombinação biomolecular (k_2), será desenvolvida. A degradação (85ºC no escuro por 1000h) de células solares orgânicas, fabricadas com materiais proprietários da Heliatek GmbH, foi estudada através do uso de técnicas de caracterização básica (curva densidade de corrente – tensão, espectro de eficiência quântica externa) e transiente (fotovoltagem transiente (TPV), Suns-V_{OC}, extração de portadores de carga corrigida por circuito aberto (OTRACE), corrente limitada espacialmente por cargas (SCLC)), efetuadas no Dresden Integrated Center for Applied Physics and Photonic Materials. Resultados indicaram que a redução na eficiência das células solares, após degradação dos dispositivos, é principalmente devida a um decréscimo do *FF*, o qual é devido principalmente a uma redução da mobilidade e a resistências parasitas. Numa tentativa de abrandar o processo de degradação, a utilização de uma camada de proteção de 5nm foi também estudada. Apesar desta camada reduzir ligeiramente o *FF*, uma degradação mais lenta do J_{SC} e do *FF* compensam esta perda inicial de *FF*.

Palavras-chave: Células solares orgânicas, degradação, mobilidade, fotovoltagem transiente (TPV), extração de portadores de carga corrigida por circuito aberto (OTRACE), corrente limitada espacialmente por cargas (SCLC), Suns-V_{OC}

Index

Index of Tables

Figure Index

1 Introduction

1.1 Motivation

The growth of modern civilization demands an ever-increasing supply of energy. However, most of this energy is still produced by fossil fuels, despite their harmful consequences. [1] Recently, the development of renewable energy sources has gained more traction due to increased environmental awareness and the fact that fossil fuels are finite and dwindling resources. [2,3] Among these new eco-friendly energy sources, photovoltaics (PV) is perceived to have the highest potential due to the abundance of sunlight. [4]

Inorganic PV technology has reached a mature state, with efficiencies of around 25% for monocrystalline silicon and the highest values of 46% for multi-junction solar cells combined with a solar concentrating optical element. [5] However, this technology is responsible for less than 1.4% of the total global final energy consumption. [1] The high costs associated with production, installation and maintenance have considerably slowed the expansion of this technology in the global energy market.

Organic photovoltaic (OPV) technology presents itself as a viable cost-effective solution. The advantages of using synthetic organic materials include low production costs, large area production of lightweight and flexible modules using non-toxic materials and compatibility with high throughput roll-to-roll manufacturing. [6] Since the first organic planar heterojunction device in 1986 by Tang [7], the efficiency has risen from 1% up to 13.2%, the current world record, as reported by Heliatek GmbH [8]. OPVs are currently on the edge of competing with other technologies, particularly in applications such as automotive, building integrated photovoltaics (BIPV) or applications requiring flexible surfaces (Figure 1).

Figure 1 – Heliatek projects demonstrate applications such as photovoltaics for the automotive industry (left), BIPV applications (center) or modules on flexible surfaces (right). Pictures from [9]

In order to achieve the successful commercialization of this technology, its efficiency must be further increased. The *power conversion efficiency* (*PCE*) of a photovoltaic device is proportional to the product of the *short-circuit current density* (J_{SC}), *open-circuit voltage* (V_{OC}) and *fill factor* (*FF*). [10] J_{SC} depends mainly on the fraction of absorbed solar photons, and values of 15-20 mA/cm^2 (for standard reporting conditions – Sec. 2.2.2) are currently considered efficient. [11] V_{OC} depends on the energy levels of the chosen materials and the recombination rate of the photo-generated charge carriers. Values of around 1.1 V are currently considered high. [12] Finally the *FF* depends on transport properties quantified by the charge carrier mobilities. Currently, mobility values are rather low for organic materials ($< 10^{-3}$ cm^2/Vs), leading to accumulation of charges in the active layer, which itself leads to significant recombination losses, reducing *FF* and therefore limiting efficiency. [13] Currently, *FF* values of 80% are considered high. [14]

As the above mentioned parameters depend on the competition between the extraction and recombination of photo-generated charge carriers, fundamental research and new approaches for studying these processes, are of utmost importance to reveal new strategies for improving the efficiency of OSCs further.

1.2 Theory

1.2.1 A Comparison between Organic and Inorganic Semiconductors

Molecular Structure of Organic Materials

Organic molecules are mostly composed of carbon and hydrogen atoms. It is due to the overlap of their atomic orbitals that molecular orbitals are formed, in which electrons are delocalized. The *highest occupied molecular orbital* (HOMO) and the *lowest unoccupied molecular orbital* (LUMO) are analogous to the valence and conduction bands, respectively, of inorganic materials. [15]

Inorganic materials show a high dielectric constant ($\epsilon_r = 13\ldots16$) [16], in comparison with organic materials ($\epsilon_r = 3\ldots6$) [10], thus implying, for the latter materials, a higher Coulomb attraction force for electric charge carriers of opposing sign. This results in high exciton (electron-hole pair) binding energies (0.1 eV to 0.5 eV) [15] in comparison to inorganic materials (< 25 meV), and in small distances between positive and negative charges (few Å), created directly after photogeneration. This fundamentally changes organic device properties, since the thermal energy at room temperature (≈ 25 meV) is insufficient to dissociate excitons, thus requiring a donor-acceptor heterojunction to dissociate them into free carriers (Sec. 1.2.2).

Inorganic materials can form highly-ordered crystals, thus leading to a band transport mechanism. Due to the low order and large molecule size of organic materials the electron wave-functions are more localized, therefore the mean free path of charge carriers is in the range of the intermolecular distance. As such, charge transport is more accurately described by a hopping mechanism, resulting in lower mobilities. [10,17]

In general, the mobility (μ) defines the achievable drift velocity v_d of a charge carrier for a given electric field F (Eq.(1.1)):

$$v_d = \mu F \tag{1.1}$$

The mobility values for inorganic materials are quite high (around 10^3 cm^2/Vs for electrons in Si) [16] in comparison with organic materials (from 10^{-7} to 10^{-3} cm^2/Vs). [18,19] Furthermore, depending on the organic material, the mobility can also be strongly affected by other parameters, such as temperature (affecting the energy of the charge carriers) and charge carrier density (affecting the availability of sites), as described by several models. [20–22]

1.2.2 Organic Solar Cells

Donor-Acceptor Heterojunction

In the case of inorganic materials the thermal energy at room temperature (≈ 25 meV) is enough to dissociate an exciton, for organic materials however, a donor-acceptor (DA) heterojunction is required, as explained below. The material with the higher HOMO is the *electron donor* (D), whereas the one with the lower LUMO is the *electron acceptor* (A), and exciton generation can occur in both.

The conversion of light to electrical energy is achieved as described by the five steps shown in Figure 2. First, photons are transmitted through a transparent contact until they reach the active layer, where they are absorbed. Upon absorption of a photon, an exciton is generated in either the donor or acceptor phase (i), which then migrates to the donor-acceptor interface (ii), thus forming a *charge-transfer* (CT) state due to the energetic differences between the donor and acceptor materials (iii). In this state, the charges are separated with the electron on the acceptor and the hole on the donor, but recombination of electron and hole is still possible. This process is called geminate recombination. CT state dissociation, i.e. further migration of electrons and holes in their respective domains, away from the interface, separates the charges further. The now free charge carriers are able to move to their corresponding contacts (iv), where they are collected and extracted (v) as a useful form of electrical energy by an external circuit. [10,23]

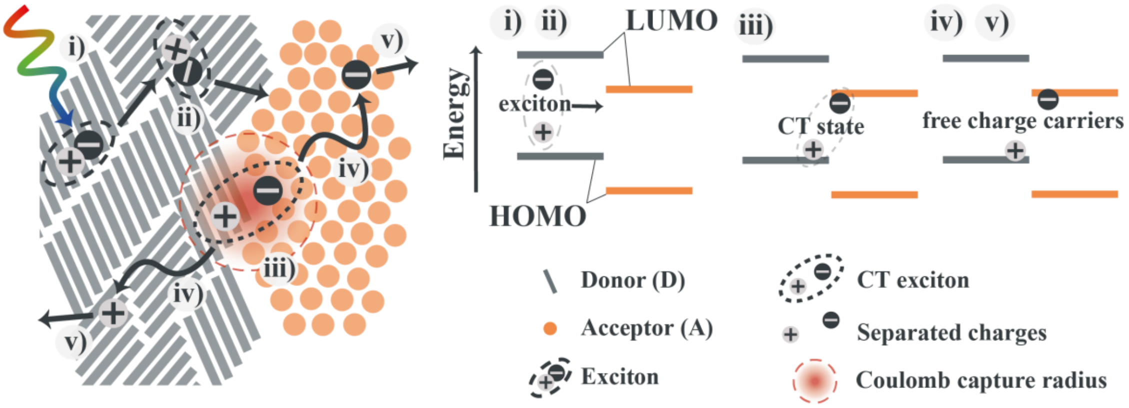

Figure 2 – The process of light conversion in a DA heterojunction, with its energy diagram on the top right. The case where an exciton is generated in the donor phase is here considered.

In order obtain an efficient implementation of a heterojunction, it is necessary to guarantee that excitons are able to reach a donor-acceptor interface within their lifetime. This implies that material phase dimension must be adapted to the exciton diffusion length, usually of few nanometers. [24]

The *flat heterojunction* (FHJ) in Figure 3(a), consists of a simple planar interface, as such, it presents good transport characteristics, since the carriers travel through the neat material phases, with low probability of meeting a carrier of opposite sign followed by recombination. This typically results in a high *FF*(Sec. 1.2.2 - *Organic Solar Cell Characteristics*). However there is a trade-off between active layer thickness (*ergo* absorption) and exciton diffusion length (~ 10nm), which is much shorter than the absorption depth (~ 100nm). [25] To overcome this limitation, another implementation known as *bulk heterojunction* (BHJ) is available. Here the active layer is composed of a DA mixture of a certain stoichiometry, thus spreading interfaces in the whole active layer volume, reducing the distance an exciton must travel to reach an interface. This allows for thicker devices (more absorption), however it implies poor transport properties (low *FF*– Sec. 1.2.2 - *Organic Solar Cell Characteristics*), as isolated carriers cannot be extracted, and the probability for electrons and holes to meet increases significantly. A hybrid of both configurations, dubbed *planar-mixed heterojunction* (PMHJ), is commonly used since it partly combines the advantages of both FHJ and BHJ (Figure 3(b)). [26] It is also possible to integrate several OSCs together (in series or parallel) into what is called a tandem solar cell (Figure 3(d)), thus enabling higher efficiencies for each successive cell stack. [27] A more novel concept, the cascade OSC, allows for a simple way of broadening of the absorption spectrum by incorporating additional photoactive materials in the active layer. [28]

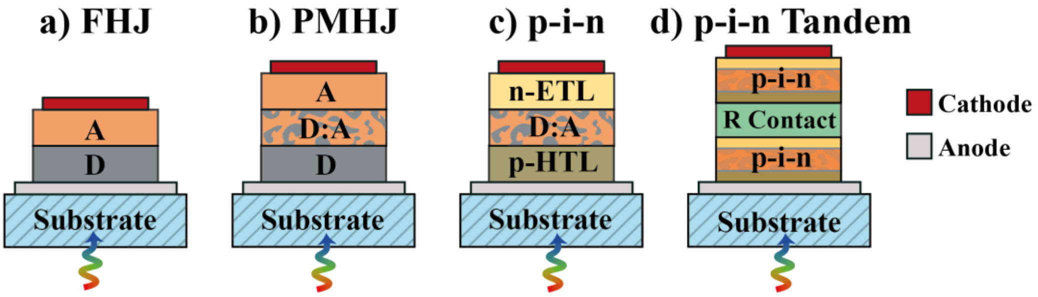

Figure 3 – Several structures with diferent types of heterojunction implementations. (a) flat heterojunction (b) planar-mixed heterojunction (c) p-i-n with BHJ intrinsic layer (d) Tandem OSC composed of two p-i-n sub-cells connected in series by a recombination contact.

The p-i-n concept

An ideal OSC structure contains an absorber and two semipermeable layers which filter electrons and holes to their respective contacts. [29] The *p-i-n* structure (Figure 3(c)) fulfills this requirement, in which the *i*-layer corresponds to an intrinsic absorber layer (in contrast to inorganic materials, where doping is often required) and the *p* and *n* correspond to a p-type doped layer (*hole transport layer* (HTL)) and an n-type doped layer (*electron transport layer* (ETL)). Doping allows for higher conductivities as well as ohmic contacts between the electrodes and transport layers. These layers are also composed of wide-gap materials to prevent absorption of solar photons by the doped layers, resulting in fast electron quenching, without the generation of free charge carriers.

Due to the fact that light is reflected at the metal back contact, an optical interference pattern is created, and thus the thickness of the doped layers can be adjusted to position the absorber layer at the point of maximum constructive interference. [30] This is possible only because OSCs are thinner than the coherence length of sunlight. [31]

An inverted p-i-n structure is also commonly used, dubbed n-i-p. This is because the n-i-p structure has a C_{60} underlayer which offers crystallization seeds for the afterward evaporated C_{60} from the BHJ blend. However, heating the substrate is also required to activate the crystallization process of C_{60}, thus forming highly pure crystalline agglomerates of C_{60}. Crystalline C_{60} has a higher electron mobility, thus enhancing charge carrier delocalization, therefore an increase in the *FF* parameter of n-i-p OSCs can be observed. [32]

Organic Solar Cell Characteristics

In the ideal, high mobility case, and under dark conditions, the characteristic behavior (JV curve) of an OSC is identical to that of a diode (Figure 4), as such the *dark current density* (J_{dark}) of an ideal solar cell (series resistance, $R_s = 0$; and shunt resistance, $R_{sh} = \infty$) is given by the Shockley equation:

$$J_{dark} = J_{rec} = J_0 \left\{ \exp\left(\frac{qV_{ext}}{n_{id} k_B T} \right) - 1 \right\} \tag{1.2}$$

Where V_{ext} is the external voltage, J_0 is the saturation current density at negative bias voltage and n_{id} is the ideality factor, which gives information on the dominant recombination mechanism, for $n_{id} = 1$ it is direct recombination, for $n_{id} = 2$ it is Shockley-Read-Hall recombination and for $n_{id} = 2/3$ it is Auger recombination. [33] In the ideal case, under illumination, the JV curve is shifted by the photocurrent $J_G = qLG$, where L is the active layer thickness and G is the photogeneration rate per unit volume.

For low mobility organic solar cells, under illumination, the Shockley equation must be adjusted, as shown by Würfel *et al.* [33] This is due to significant charge carrier accumulation caused by poor transport properties. This is not taken into account in the derivation of the original Shockley equation as it assumed high mobility inorganic materials. As a consequence, the separation of the quasi-Fermi levels in the active layer (internal voltage (V_{int})) is substantially different from the external voltage (V_{ext}).

The model proposed by Würfel *et al.* [33] considers these charge transport limitations by relating J and V_{ext} to the Fermi-level splitting, and assuming that the quasi-Fermi levels for electrons and holes exhibit the same and constant gradient within the active layer. As such, in Eq.(1.2), V_{ext} is replaced by V_{int} and the former is now defined as:

$$V_{ext} = V_{\text{int}} + \frac{L}{\sigma} J \tag{1.3}$$

Where L is the active layer thickness and V_{int} is the internal voltage. The transport properties are taken into account in the electrical conductivity (σ) parameter of Eq.(1.3), which can be derived to depend on the mobility (μ) and the Fermi level splitting (V_{int}) as:

$$\sigma = 2q\mu_{eff} n_i \exp\left(\frac{qV_{\text{int}}}{2k_B T}\right) \tag{1.4}$$

Where $\mu_{eff} = \sqrt{\mu_n \mu_p}$ is the effective mobility and n_i the intrinsic carrier density. If μ, n_i and J_0 are known, a prediction of the characteristic curve becomes possible. Where $J_0 = qLk_2 n_i^2$, with k_2 defined as the bimolecular (second order) nongeminate recombination coefficient. With knowledge of the characteristic curve, the *PCE* can be derived, as the *output power density* (P) is given by $P = -JV$. The most important parameter of a solar cell combines the aforementioned parameters into the *power conversion efficiency* (*PCE*):

$$PCE = \frac{J_{SC} V_{OC} FF}{P_{illu}} \tag{1.5}$$

Where P_{illu} is the illumination power density (100 mW/cm^2 in accordance with standard reporting conditions – Sec. 2.2.2). In Eq.(1.5), the *short-circuit current density* (J_{SC}) is obtained at zero voltage ($J(V_{ext} = 0)$). Whilst the voltage at which there is no net current flow (*open-circuit voltage* (V_{OC})), is obtained by setting $J = 0$, at which $V_{ext} = V_{int}$. Finally, the *maximum power output* (*Pmax*) contributes to the definition of the *fill factor* (*FF*):

$$FF = \frac{P_{\max}}{J_{SC} V_{OC}} \tag{1.6}$$

This value is dimensionless and is intended as a figure-of-merit of the device, a low value is associated with bad transport properties, such as low mobilities [34], energetic barriers [35], high series resistance (R_s) or low shunt resistance (R_{sh}).

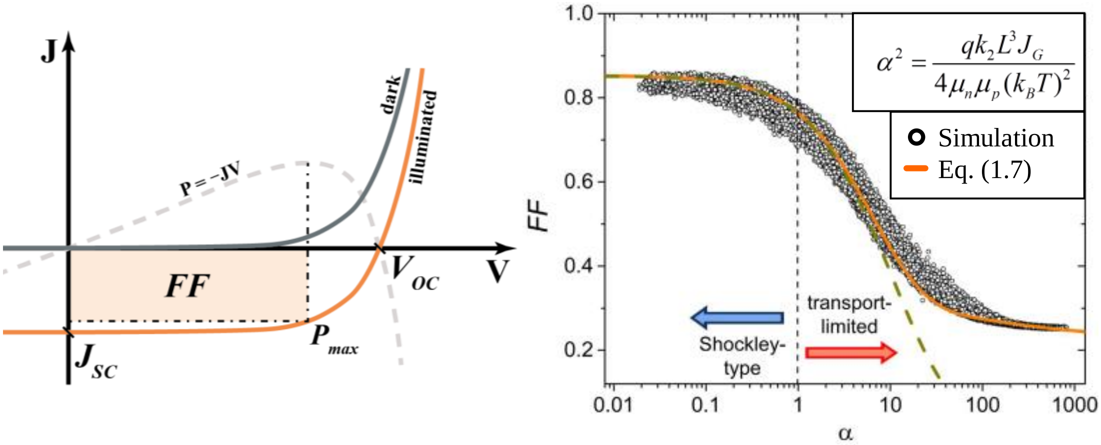

Figure 4 – Left: Characteristic curve of a solar cell and a visual representation of its performance parameters. Right: Open circles represent simulated JV-curves with balanced mobilites and V_{OC} between 0.7 and 0.9 V. The solid line represents FF-α dependency according to Eq. 1.7, whereas the dashed line represents the definition of FF from which the empirical Eq. 1.7 was based on. Adapted from [38]

Recently, Neher *et al.* introduced a new figure of merit (α) [36], expressing the balance between free charge recombination and extraction in photoactive materials with low mobilities. Under the assumptions of balanced mobilites (thus avoiding space charge effects), as well as realistic illumination conditions ($J_0 \ll J_G$), an empirical expression for *FF* was found:

$$FF = \frac{u_{OC} - \ln(0.79 + 0.66u_{OC}^{1.2})}{u_{OC} + 1} \tag{1.7}$$

With $u_{OC} = \frac{qV_{OC}}{(1+\alpha)\,\mathrm{k}_B T}$, thus describing the $FF(V_{OC})$ dependence (Figure 4). In this expression, α is defined as follows:

$$\alpha^2 = \frac{qk_2L^3J_G}{4\mu_n\mu_p(k_BT)^2} \tag{1.8}$$

Thus relating α to the generation current density (J_G), the active layer thickness (L) and mobilities (μ_n and μ_p). Should α be larger than 1, photocurrents become strongly transport-limited, therefore decreasing the *FF*. According to this equation, the parameters which most affect *FF* are active layer thickness and the effective mobility. Thus this new figure of merit (α) is able to relate material properties such as charge carrier mobilities (μ_n and μ_p), active layer thickness (L) and the bimolecular recombination coefficient (k_2) to characteristic device parameters such as *FF*.

2 Materials and Methods

2.1 Production

Each production run is fabricated on a large glass substrate covered with pre-structured indium tin oxide (ITO) (Thin Film Devices, USA), with a thickness of 90nm and a sheet resistance of 30 Ω/sq. It contains 6x6 small square samples, which were later cut and individualized.

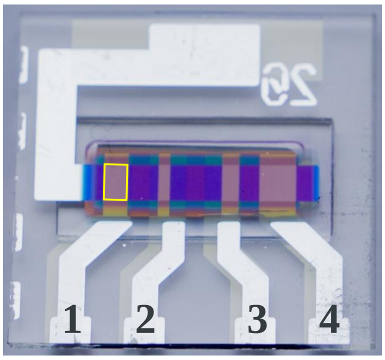

Figure 5 – Single sample containing four OSCs (pixels) of different areas. The active area of pixel 1 is highlighted.

As shown in Figure 5, each of those samples contains four cells (designated pixels) of different areas. They are glass encapsulated in an N_2 atmosphere and contain a humidity getter. The active area is defined as the area between the top and bottom contacts. Pixel areas are found in Annex C.

Both solar cell and single carrier device types were produced by thermal evaporation under vacuum. All OSCs are *n-i-p* structures, an inverted form of the previously discussed *p-i-n* structure (Sec. 1.2.2). The detailed run planning sheets can be found in Annexes D and E.

2.2 Characterization

2.2.1 EQE

The *external quantum efficiency* (EQE) is defined as the ratio of extracted charges at short-circuit by incident photons. By measuring the short-circuit signal of the OSC in dependence of the wavelength, its spectral response can be obtained, and through it the *EQE* is calculated. J_{SC} can also be obtained by integrating this spectrum. [37].

The EQE measurement setup consists of a xenon arc lamp (Appex Illuminator), a monochromator (Cornerstone 260, Newport), a chopper and a lock-in amplifier (SR725, Signal Recovery). The measurement is performed with a wavelength scan between 300 and 900 nm and a step width of 5nm. (Due to the change of filters in the monochromator an artefact peak at 600nm is visible in most measurements).

2.2.2 Characteristic Curve (JV)

The standard reporting conditions (SRC) for OSCs are a *sample temperature of 25ºC*, an *illumination intensity of 100 mW/cm*^{2} and a *defined reference illumination spectrum* (generally AM1.5G) [38]. As it is difficult to exactly reproduce an AM1.5G spectrum, a spectral *mismatch factor* (MM) must be considered. [10,37] From the dark JV curves, R_S and R_{Sh} can also be respectively estimated by linear fits in the high current forward direction area, and in the area around J_{SC}.

The characteristic curve measurement setup consists of a xenon lamp (16S-003-300, Solar Light Company Inc.) serving as sun simulator, optical fibers, a reference silicon photodiode (S1337-33BQ, Hamamatsu) and a Keithley SMU2400. V_{OC} is obtained from a linear interpolation of the two points closest to $J = 0$ mA/cm^2. J_{SC} is corrected for the effective area of each device. *FF* is calculated according to Eq. (1.6). This measurement is performed autonomously and assumes a single MM for all samples, whose value is taken from the average of all MM's determined by the EQE technique. [37].

2.2.3 TPV

A *transient photovoltage* (TPV) measurement allows for the determination of charge carrier lifetimes (τ). The OSC is held at open-circuit (OC) conditions under a constant bias light, upon which a transient voltage ΔV (< 5 mV, to avoid influencing steady-state conditions [34]) is induced by a light pulse. Due to the OC conditions no charge carriers are extracted, thus they must recombine within the device and the single exponential TPV decay is used as a measure of the charge carrier lifetime (τ), where $\Delta V_{OC} \propto \exp(-t/\tau)$. [39] An example of the fit can be found in Annex G.

The setup consists of a metal box (allowing for low noise measurements due to reduced external electromagnetic influences), a high power LED (LZP-D0CW0R-0065, LED Engin), its corresponding lens (LLNF-3T11-H, LED Engin), an HP Agilent Technologies 33600A waveform generator, a power supply unit (PSU) (Elektro-Automatik EA-PS 3032-20B), a Keithley SMU2400, a Tektronix 54815A digital storage oscilloscope and a picosecond laser system (Ekspla PL2230).

In the framework of this thesis, a modification was done to run a pulsed TPV measurement, therefore reducing the heating induced by the bias light and allowing for measurements with higher light intensity, thus reaching higher voltages.

2.2.4 SCLC

The space-charge limited current (SCLC) measurement is performed on the dark-IV curves of single-carrier devices, in which unipolar transport occurs (selective injection of a single type of charge carrier). Fitting of the IV curve with the appropriate equation enables the measurement of mobility values for electrons and holes separately. The setup consists of a metal box identical to the one mentioned in the TPV technique and a Keithley SMU2400.

This technique requires “good” contacts (i.e. selective and ohmic), so as to ensure unipolar transport and a negligible voltage drop at the injection contact, respectively. Otherwise, the injection contact acts as an unquantifiable resistance connected in series with the actual device. [40] In case of “good” contacts, the data presents a slope of 2 in a double logarithmic plot (Annex F), and by fitting the Mott-Gurney (MG) equation (similar to Eq. (1.9) but assuming $\gamma = 0$), the mobility can be extracted. However, if the mobility has a strong field dependence, a fit with the Murgatroyd (Mt) equation (Eq. (1.9)) is more correct, in which case a slope higher than 2 should be observed, for higher voltages, in the plot.

$$J = \frac{9}{8}\frac{\varepsilon_0 \varepsilon \mu_0}{L^3} V^2 e^{0.89\gamma\sqrt{V/L}} \tag{1.9}$$

Where ϵ_r is the dielectric constant (a value of 4 was used), μ_0 is the mobility at low field, L is the active layer thickness and γ is the field dependence of the mobility.

Although this is a straightforward method that gives both the electron and hole mobility, it requires the fabrication of specialized single carrier devices, as well as an ideal injection of charges (“good” contacts). Additionally it is dependent on a model, which in the Murgatroyd case, has two fitting parameters.

2.2.5 OTRACE

The open circuit corrected charge carrier extraction (OTRACE) technique is an improvement of the commonly used photo-charge extraction by linearly increasing voltage (photo-CELIV) method. [41] It differs in the sense that a time dependent offset voltage is applied during the delay time between the photogeneration pulse and charge extraction, thus ensuring open-circuit conditions during charge carrier recombination. [42,43] A measurement of the bimolecular recombination coefficient (k) can be obtained as well as for mobility. Parameters from Eq. (1.10) are determined from the extraction curve (Annex I).

$$\mu = \frac{L^2}{2A' t_{\max}^2}\left[\frac{1}{6.2+\left(1+0.002\frac{\Delta j}{j_0}\right)}+\frac{1}{1+0.12\frac{\Delta j}{j_0}}\right]^2 \tag{1.10}$$

Where L is the active layer thickness, A' is the slope of the applied voltage pulse, t_{max} is the position of the maximum peak of the current transient, and $\Delta j/j_0$ is the magnitude of the photocurrent response. Its setup is similar to the TPV technique, with an identical metal box, the Tektronix 54815A digital storage oscilloscope and the HP Agilent Technologies 33600A waveform generator.

Although this technique does not require special devices and shows the dependence of mobility on charge carrier density, it still relies on a model and requires thick samples with a small active area since it is prone to RC limitations.

Other methods for measuring mobility are available, in particular, POEM (electric potential mapping by thickness variation) is model free, however it requires the use of an extensive number of samples. [19]

2.2.6 Suns-V_{OC}

This measurement was initially introduced for inorganic materials by Sinton and Cuevas in 2000. [44] Its applicability in OSCs was later investigated in 2013 by Schiefer et al. [45] An improvement of this technique was made, whereby instead of a decaying flash, a stepped light intensity is used, where each step is long enough to ensure that a quasi-steady state is reached. This method does not require fast recombination processes, which avoids the need for a generalized analysis.[46]

In this technique, the OSC is illuminated from low to high intensities, and at each intensity step its V_{OC} and the illumination intensity are measured. This procedure is then repeated but J_{SC} is measured instead of V_{OC}. The obtained V_{OC} (intensity) and J_{SC} (intensity) curves are then combined to obtain pseudo-JV curves, i.e., characteristic curves whose generation and recombination mechanics are unaffected by the series resistance (R_S) neither by the transport resistance (R_{tr}) of the photoactive layer. [45] This technique allows for the determination of the ideality factor (n_{id}) according to Eq. (1.11).

$$n_{id} = \frac{q}{k_B T} \frac{\partial V_{OC}}{\partial \ln(\mathrm{J}_{SC})} \tag{1.11}$$

Where V_{OC} and J_{SC} are the open-circuit voltage and short-circuit current density taken from the pseudo-JV curves. Additionally, together with a 1 sun JV curve and R_S, the intrinsic carrier density (n_i) can also be determined using Eq. (1.12), as shown by Schiefer et al. [47]

$$n_i = \frac{L}{R_{tr}(J) \cdot 2q \cdot \mu_{eff} \cdot \exp\left(\frac{q \cdot V_{Suns}}{2k_B \cdot T} \right)} \tag{1.12}$$

Where L is the active layer thickness, $R_{tr}(J)$ is the transport resistance caused by the motion of charge carriers through the photoactive layer, μ_{eff} is the effective mobility and V_{Suns} is the voltage difference between the pseudo and 1sun JV curves.

Although Suns-V_{OC} may not be as reliable as the J_{SC}-V_{OC} method presented by Wolf and Rauschenbach [48], since the former relies on the assumptions that J_{SC} scales linearly with light intensity and that $J_{Gen} \approx J_{SC}$, it is much easier and faster to perform than the latter. It is however, enough for a qualitative comparison of samples, as is intended in this thesis. Its setup consists in a metal box, three Keithley SMU2400's, two power supply units (Elektro-Automatik EA-PS 3032-20B) and a Newport 818 photodetector.

3 Results and Discussion

Two runs (6x6 substrate) of devices were characterized, their detailed planning sheets are in Annex D and Annex E. Each run contains 12 samples of each device type (*electron-only*, *hole-only* and *OSC*) and each sample contains 4 pixels of different areas, thus totaling 144 devices per run. There are two different types of device layouts, as represented in Figure 6. Short designations for sample and pixel are hereby defined as *s* and *p*, e.g., *s11p4* refers to pixel 4 of sample 11, as highlighted in green in Figure 6.

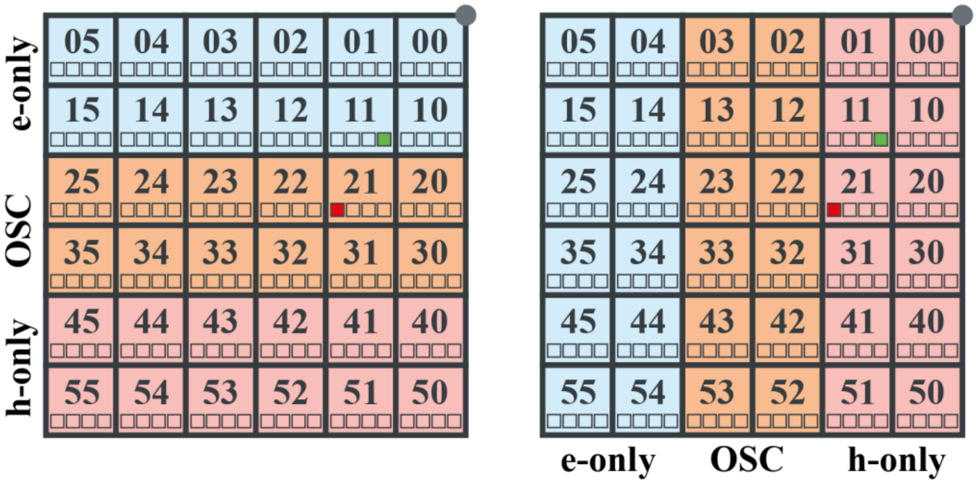

Figure 6 – Device layout for the first run (left) and for the second run (right). Pixel numbering consists of 1 to 4 from left to right. Highlighted in green and red are *s11p4* and *s21p1*, respectively.

Green pixels (*s11p4*) represent accepted measurements, red (*s21p1*) represents outliers, and no coloring (remaining pixels) represents failed measurements. As the EQE and JV measurement processes are automated, an optical fiber scans the OSC in search of the best position for maximum illumination. This procedure was designed for a standardized pixel size of 6.44 mm^2 (*p4*), however, the remaining pixels have smaller sizes, thus the optimization routine may fail in such cases (generally *p2* or *p3*). Samples may also cease to work due to failure of the encapsulation, resulting in uncontrolled degradation. These are some of the reasons why measurements may fail and are represented with no coloring. As a safeguard against these events, sample redundancy is included in the second column/row of each device type, e.g., *s00* and *s10* are replicas in the left layout, whilst *s00* and *s01* are replicas in the layout on the right.

Some sample characteristics (V_{OC}, J_{SC}, *FF* and *PCE*) were subjected to statistical treatment. Firstly, outliers were rejected in accordance with *Peirce's criterion*, as described by Ross. [49] Interval plots were made, where the vertical error bars represent a 95% confidence interval (CI) for the mean, as calculated by a *one-sample t test* for the mean. [50]

The stacks and thicknesses (Figure 7) are identical for all runs, with exception of the intrinsic layer, whose materials, blending ratios and thicknesses are varied with and within each run. These standardized *n* and *p* layers imply that the optical interference pattern is not optimized for each thickness.

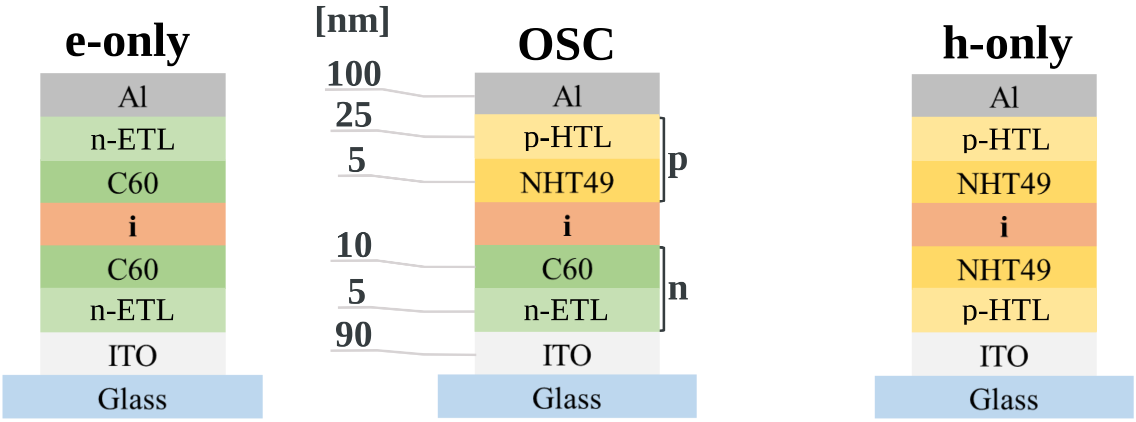

Figure 7 – Material stack for each device type. From left to right, electron-only devices (*n-i-n*), organic solar cells (*n-i-p*) and hole-only devices (*p-i-p*). The thicknesses of the *n* and *p* sub-stacks for the single carrier devices are identical to the ones indicated in the OSC devices.

Materials with the designations NHT (Novaled Hole Transporter), HDR (Heliatek donor red) and HDG (Heliatek donor green) are proprietary materials and thus their structures are undisclosed. The p-HTL and n-ETL layers are doped blends of transport materials. However, the exact chemical structures are irrelevant for studying the effect of absorber batch purity, degradation and device architecture on the carrier mobility, recombination rate and their influence on device performance.

3.1 The first run – A comparison of batch purity

In this run a purity comparison was performed. The active layer of HDR14 (donor) blended with C_{60} (acceptor) was synthesized by Heliatek GmbH using two different approaches, resulting in two different purities of this material. As determined in the work done previously by Sascha Ullbrich, Johannes Benduhn, Dr. Donato Spoltore and Prof. Dr. Koen Vandewal, the two synthesis methods yielded materials with differing characteristics and were divided into a good and a bad batch.[1]

3.1.1 Degradation of the first run

In the context of this thesis, the aforementioned work was continued, with a focus on degradation. The run was degraded in an oven at 85ºC for 1000h in the dark. The intention was to observe the effect of degradation on device performance, as well as to see if the bad and good batch were degraded differently. A reduction in the device performance characteristics was expected.

External Quantum Efficiency

The EQE spectra of *s31-34p4*, before and after degradation, can be found in Figure 8. The degraded samples present identical spectra to the pristine ones. Thus this measurement indicates no change in J_{SC} due to degradation.

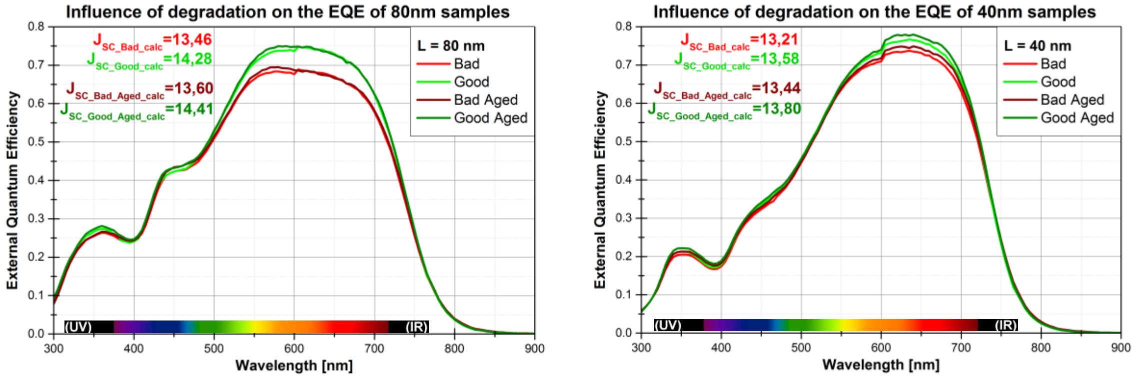

Figure 8 – EQE spectra of *s31p4* (80 nm - Bad), *s32p4* (40 nm - Bad), *s33p4* (40 nm - Good) and *s34p4* (80 nm - Good), before (light colors) and after degradation (dark colors). The bad batch is represented in red and the good batch in green.

---

[1] *EQE* and *SCLC* measurements of pristine samples were done by Dr. Donato Spoltore and *JV*, *OTRACE*, *TPV* and *Suns-*V_{OC} measurements of the same samples were done by Sascha Ullbrich.

Characteristic Curves

The characteristic curves of the same OSCs can be found in Figure 9. While there may appear to be an increase in J_{SC} due to aging, particularly for the 40 nm samples, this is within the variations caused by the fluctuating light intensity of the xenon lamp, thus these minor changes are insignificant. V_{OC} remains constant after degradation for all samples. In terms of *FF* both the 80 and 40 nm samples reveal a reduction due to degradation. Table 1 presents a summary of these characteristics together with the parasitic resistances.

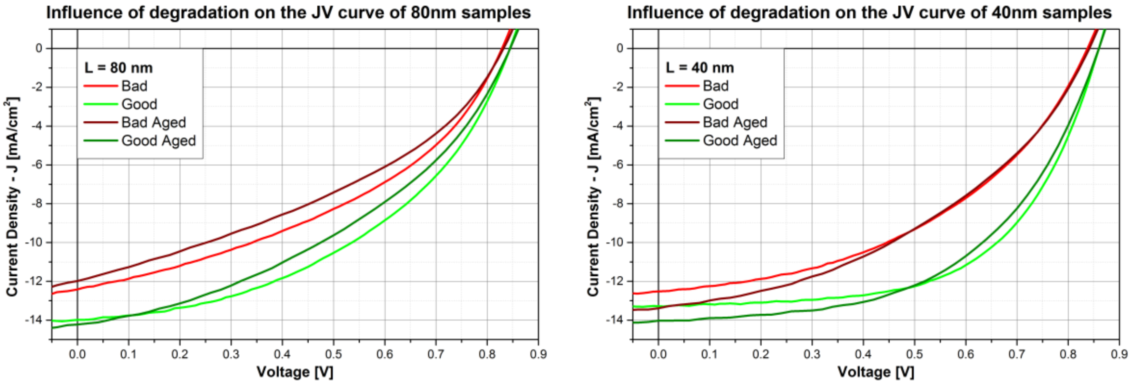

Figure 9 – JV curves of *s31p4* (80 nm - Bad), *s32p4* (40 nm - Bad), *s33p4* (40 nm - Good) and *s34p4* (80 nm - Good), before (light colors) and after degradation (dark colors). The bad batch is represented in red and the good batch in green.

It may appear that the good batch degrades slightly more than the bad one, however, statistical treatment of a larger number of samples would be necessary to draw firmer conclusions. As a result, the *PCE* also decreases by approximately 10%, but apparently only for the 80 nm samples. The fluctuations of J_{SC} in the 40nm samples can explain why an expected *PCE* reduction is obscured.

Table 1 – Performance characteristics of the aforementioned samples. Red and green indicate a significant decrease or increase, respectively, and black no significant change. Percentual changes are relative.

Batch	**L [nm]**	**Condition**	J_{SC} **[mA/cm²]**	V_{OC} **[V]**	***FF*** **[%]**	***PCE*** **[%]**	R_S **[Ω]**	R_{Sh} **[MΩ]**
Bad	**80**	**Unaged**	12,41	0,829	41	4,20	8	3,00
			-3%	**≈ 0%**	**-8%**	**-11%**	**73%**	**-85%**
		Aged	11,98	0,831	38	3,73	14	0,46
	40	**Unaged**	12,52	0,837	45	4,71	9	3,39
			7%	**≈ 0%**	**-8%**	**-1%**	**41%**	**-93%**
		Aged	13,39	0,841	42	4,67	13	0,23
Good	**40**	**Unaged**	13,28	0,860	59	6,72	7	7,56
			6%	**≈ 0%**	**-9%**	**-4%**	**64%**	**-91%**
		Aged	14,03	0,860	53	6,43	11	0,67
	80	**Unaged**	13,98	0,844	46	5,37	7	8,26
			2%	**≈ 0%**	**-11%**	**-10%**	**82%**	**-53%**
		Aged	14,23	0,844	40	4,84	13	3,90

SunsV$_{OC}$

The ideality factor characterization of the same samples can be found in Figure 10. Recalling Eq. (1.11), and as observed in this characterization there is no change in n_{id}, thus implying no change in the recombination mechanism after degradation.

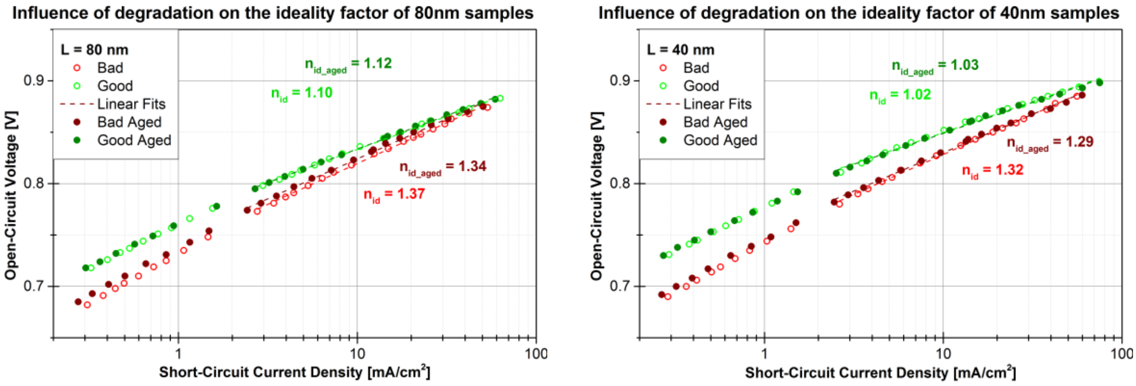

Figure 10 – Ideality factor characterization of *s31p4* (80 nm - Bad), *s32p4* (40 nm - Bad), *s33p4* (40 nm - Good) and *s34p4* (80 nm - Good), before (light colors) and after degradation (dark colors). The bad batch is represented in red and the good batch in green.

Transient Photovoltage

The charge carrier lifetime characterization for the same samples can be found in Figure 11. The lifetime plots are identical before and after ageing, thus the measurement implies that there is no change in the recombination constant. Recalling that the recombination mechanism also did not change, these measurements support the finding that no change in V_{OC} has occurred.

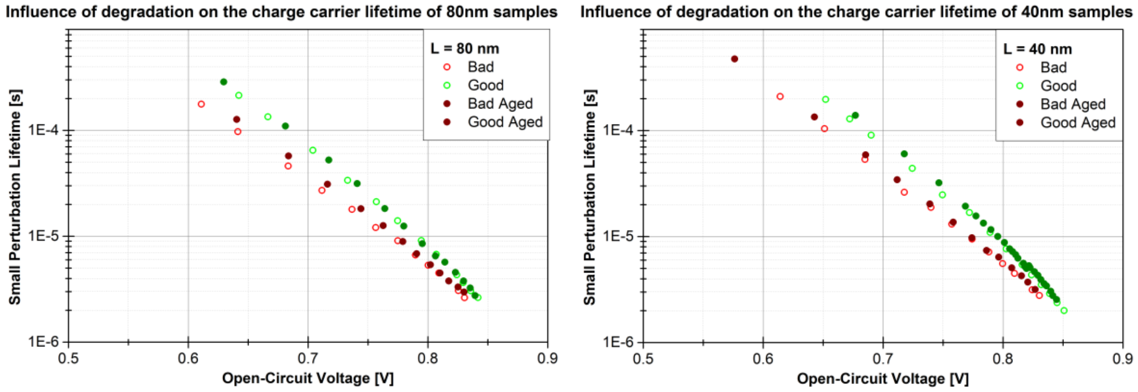

Figure 11 – Charge carrier lifetime characterization of s31p4 (80 nm - Bad), *s32p4* (40 nm - Bad), *s33p4* (40 nm - Good) and *s34p4* (80 nm - Good), before (light colors) and after degradation (dark colors). The bad batch is represented in red and the good batch in green.

OTRACE and SCLC

The OTRACE mobility measurements for *s31p2* and *s34p2* can be found in Figure 12 on the left side. Samples of lower thickness were not included due to RC limitations. As mobility measurements usually present values with high variability, the OTRACE results can be interpreted as no change in mobility due to degradation.

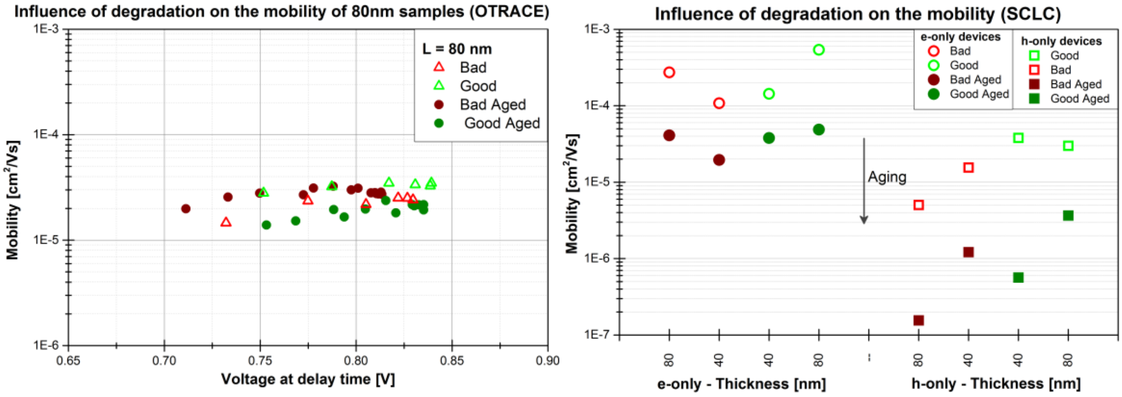

Figure 12 – Left: OTRACE mobility measurements for *s31p2* (80nm - Bad) and *s34p2* (80nm - Good) before and after degradation. Right: SCLC for the electron mobilities of *s11p4* (80nm - Bad), *s12p4* (40nm - Bad), *s13p4* (40nm - Good), *s14p4* (80nm - Good) and for the hole mobilities of *s41p4* (80nm - Bad), *s42p4* (40nm - Bad), *s43p4* (40nm - Good) and *s44p4* (80nm - Good).

The SCLC mobility measurements fitted with the Murgatroyd model for *s11-14p4* (e-only) and *s41-44p4* (h-only) are presented in Figure 12 on the right side. This measurement indicates a mobility drop of approximately one order of magnitude, for all samples after degradation. This is inconsistent with the OTRACE results, which could be due to a different aging of the single carrier devices, or most likely, non-ideal injection of charges due to degradation. Since in the OTRACE technique the carriers are generated instead of injected, the mobility of the active layer is measured and thus no injection problems should be noticeable.

SunsV_{OC} - n_i

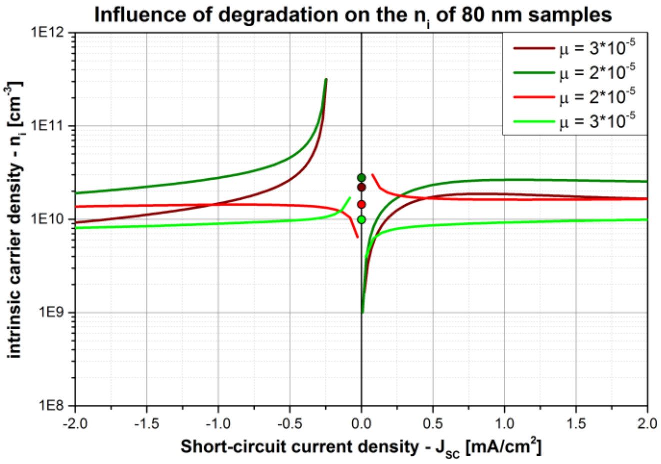

Figure 13 – Intrinsic carrier density plot of *s31p4* (80 nm - Bad) and *s34p4* (80 nm - Good) before (light colours) and after degradation (dark colours)

In Figure 13 the intrinsic carrier density plot of *s31p4* and *s34p4* can be observed. As the model of this measurement suggests that a higher mobility leads to a lower n_i, an accurate measurement of the latter is dependent on the accurate measurement of the former. An estimation of the n_i values is made as presented in Table 2.

Table 2 – Summary of the mobilities, recombination constant and intrinsic carrier density of *s31p4* (80nm Bad) and *s34p4* (80nm Good) before and after degradation.

L [nm]	**Batch**	**Condi-tion**	**μ_{eff} – SCLC (Mt) [cm^2/Vs]**	**μ-OTRACE [cm^2/Vs]**	**k_r [cm^3/μs]**	**n_i [cm^{-3}]**
80	**Bad**	Unaged	$4\cdot10^{-5}$	$2\cdot10^{-5}$	$9\cdot10^{-13}$	$1\cdot10^{10}$
		Aged	$3\cdot10^{-6}$	$3\cdot10^{-5}$	$8\cdot10^{-13}$	$3\cdot10^{10}$
	Good	Unaged	$1\cdot10^{-4}$	$3\cdot10^{-5}$	$1\cdot10^{-12}$	$1\cdot10^{10}$
		Aged	$1\cdot10^{-5}$	$2\cdot10^{-5}$	$7\cdot10^{-13}$	$3\cdot10^{10}$

Simulation

The model parameters can be observed next to the simulations themselves, in Figure 14. Since each of these parameters can be measured, most of the obtained values (Table 3 and Table 2) were used for the simulation and a temperature of 295 K was assumed. In accordance with the model assumptions, only bimolecular recombination was taken into account (n_{id}=1) thus, n_{id} was the only measured parameter which was not used in the model.

As such, n_{id}, R_S and R_{Sh} (both of which are also not taken into account by the model), as well as measurement variability, are some of the reasons that can explain deviations between the experimental data (dotted lines) and the model projections (solid lines).

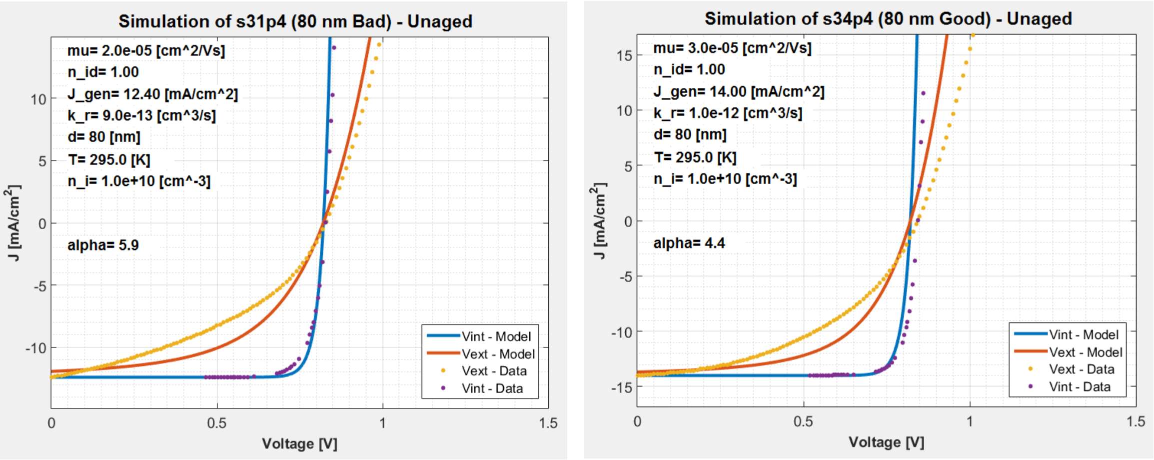

Figure 14 – Simulation of unaged *s31p4* (80 nm Bad) and *s34p4* (80nm Good) on the left and right sides respectively. Solid lines indicate a simulation based on parameters, and dotted lines indicate experimental data.

Taking into account the aforementioned causes for deviation, both simulations for unaged *s31p4* and *s34p4* are mostly agreeable. Some effect of the parasitic resistances is already visible. To obtain a better fit, values of mobility with a precision of decimal places would be required, which can not be obtained by the measurements. Simulation of the aged samples was not performed due to even higher R_S and lower R_{Sh}.

Summary

- In this run high temperature dark degradation caused no change in J_{SC}, this was confirmed by the agreeing EQE and JV measurements.

- No change was also observed in the V_{OC} according to the JV curves. Both the ideality factor from Suns-V_{OC} and the charge carrier lifetimes from TPV remained unchanged after degradation, thus supporting a constant V_{OC}.

- JV curves determined a reduction in *FF* for all samples. OTRACE indicated no change in mobility. In contrast, SCLC indicated a reduction of approximately one order of magnitude in mobility. This could have been due to a worsening of the contacts due to degradation, rendering the SCLC characterization innaccurate. Simulations revealed a reasonable fit for the unaged s31p4 (80 nm Bad) and s34p4 (80 nm Good) samples.

- Degradation in this run caused a reduction in *PCE* of approximately 10% for all samples, mostly due to a reduction in *FF*, itself due mostly to extrinsic factors, specifically an increased R_S and a reduced R_{Sh}. To ascertain a difference in degradation between the good and the bad batch a more thorough statistical analysis would be required.

3.2 The second run – Effect of a protective layer

In this run an architectural comparison is performed. The intrinsic layer is a blend of HDR087 (donor) and C_{60} (acceptor). HDR087 has been considered a material sensitive to degradation in previous tests done by Heliatek. This material is compared with an identical layer, albeit with the addition of a 5nm layer of a different small molecule:C_{60} blend (HDG232:C_{60}), hereby called the protective or added layer.

This added layer is very thin in comparison to the usual thicknesses of other active layers (40, 80 nm), thus very little impact, or none at all, can be expected on the performance characteristics of the device. However, it is expected that this added layer will help to protect the OSC against degradation, as such this study is performed in the following section, in comparison with the baseline established here.

EQE and Characteristic Curves

The basic characterization of *s12p4* (80 nm), *s23p4* (80 + 5 nm), *s32p4* (40 + 5 nm) and *s42p4* (40 nm) can be found in Figure 15. The added layer shows negligible influence in the EQE spectrum. The J_{SC} calculated by the EQE mostly matches the measured J_{SC} of each sample. Minimal deviations can be explained by the artefact peak at 600 nm (most visible for the 40 nm sample), which causes a slight over-estimation of J_{SC}. It would also be expected that the thickest samples would present higher currents due to the increased absorption, however this can be explained by the non-optimized optical field, which in this case, favours the thinner samples.

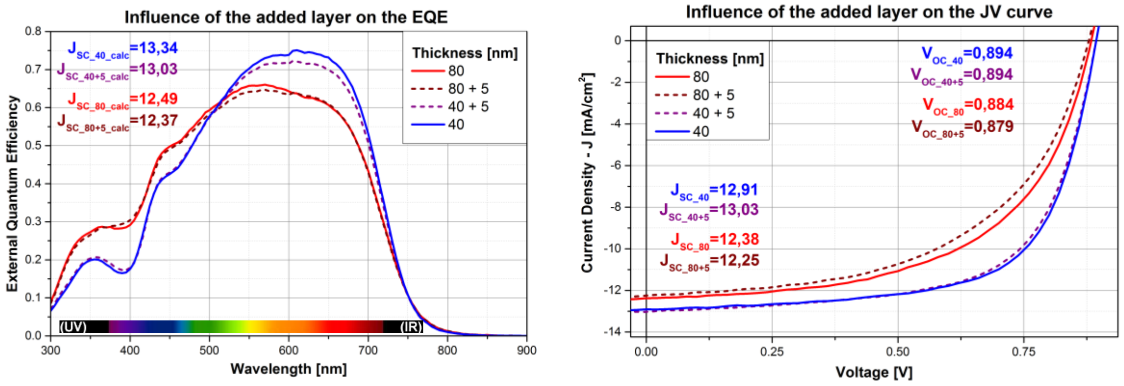

Figure 15 – EQE (left) and JV (right) curves of *s12p4* (80 nm), *s23p4* (80 + 5 nm), *s32p4* (40 + 5 nm) and *s42p4* (40 nm). Dashed and solid lines represent samples with and without layer, respectively.

By following the previously outlined statistical procedures, interval plots for the performance characteristics of the OSCs in Figure 16 were made and can be found in Figure 17. From the overview in Figure 16 the number of accepted and rejected samples can also be observed.

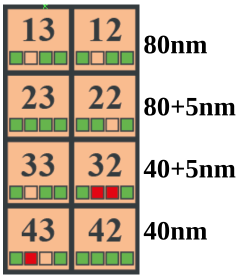

Figure 16 – Sample overview

When observing the interval plots, one can immediately conclude that J_{SC}, as well as the 40 and 40+5 nm samples have larger variabilities (from ≈6% to ≈17%), thus making their comparisons harder. The large variation of J_{SC} is due to the fluctuations in the Xe lamp. More specifically, in the interval plot of J_{SC}, a single grouping of these variables can be observed, thus suggesting that there are no significant differences of J_{SC} when comparing all samples. In the interval plot of V_{OC}, two distinct groups are observed, one for the 80 and 80+5 nm samples and another for the 40 and 40+5 nm samples.

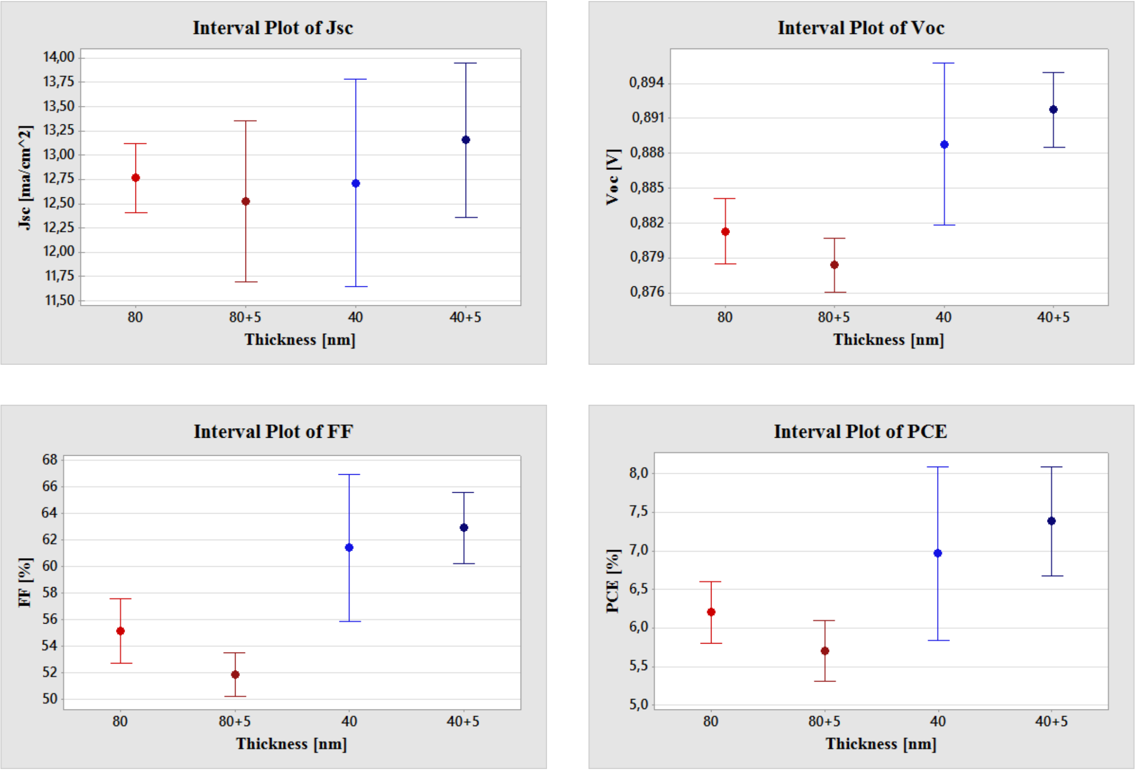

Figure 17 – Interval plots of the performance characteristics of the aforementioned samples. Vertical bars represent a 95% confidence interval for the mean value. Sample numbers (N) are of 6, 7, 5 and 6 for the 80, 80+5, 40+5 and 40 nm samples respectively.

Thinner samples present a higher *FF* than thicker ones, which is expected when recalling Eq. (1.8). According to the interval plot of *FF*, a difference can be seen from the 80 to the 80+5 nm sample, thus the added layer slightly reduces the average of the *FF*, by a maximum of around 8% (absolute). Even though no solid conclusions can be drawn from the 40 and 40+5 nm samples due to their large variabilities, a slight reduction in the *FF* for these latter should be expected, since the addition of such a thin layer of unknown roughness is a reasonable cause for added morphology and transport problems, independently of the thickness of the underlying active layer. The added layer can cause a reduction in *PCE* by a maximum of around 1,3%. Table 4 summarizes these results.

Table 4 – Summary of the OSC performance characteristics. Significant decreases are indicated in red, non-significant changes are in black. Percentual changes are relative deviations.

L [nm]	J_{SCavg} [mA/cm^2]	V_{OCavg} [V]	FF_{avg} [%]	PCE_{avg} [%]
80	12,77	0,881	55	6,2
	-1,9%	**-0,3%**	**-5,9%**	**-8,0%**
80+5	12,53	0,878	52	5,7
40	12,72	0,889	61	7,0
	3,5%	**0,3%**	**2,4%**	**6,0%**
40+5	13,16	0,892	63	7,4

Suns-V_{OC} and TPV – V_{OC}

In Figure 18 the lifetime and ideality factor characterizations of *s12p4*, *s22p4*, *s32p4* and *s42p4* are presented. The lifetime plot indicates two groups of lifetimes, one for the 80 and 80+5 nm samples and another for the 40 and 40+5 nm samples. As such, it seems the addition of the 5 nm layer has no effect on charge carrier lifetime, which implies no change in the recombination constant.

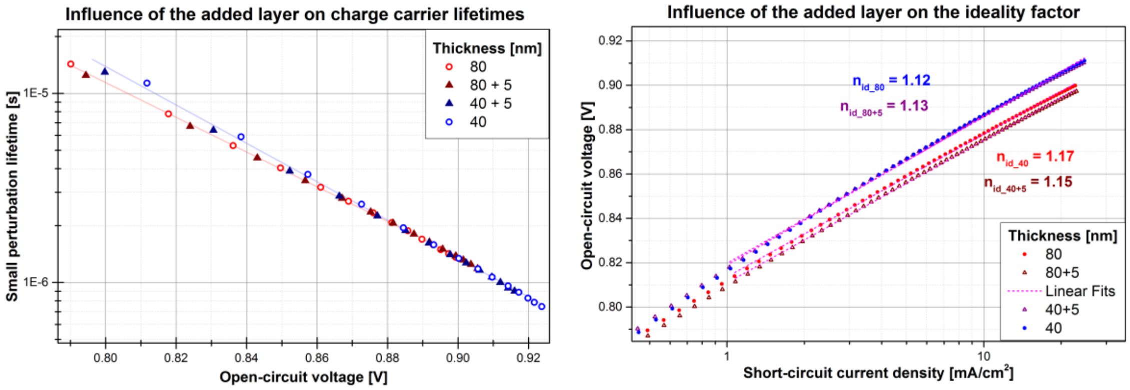

Figure 18 – Lifetime (left) and ideality factor (right) characterization of *s12p4* (80 nm), *s22p4* (80 + 5 nm), *s32p4* (40 + 5 nm) and *s42p4* (40 nm). The lifetime plot contains two coloured lines used as a visual aid.

As for the ideality factor, it has a similar grouping to the one observed in the lifetime characterization, thus suggesting no change in the recombination mechanism. As neither the ideality factor nor the charge carrier lifetimes were affected by the added layer, this implies there was no change in neither the recombination mechanism nor its constant, thus supporting that the added layer had no effect on V_{OC}.

OTRACE and SCLC

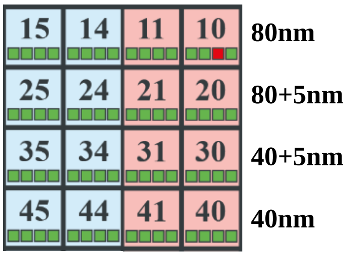

Figure 19 – Sample overview

The OTRACE measurements of *s12p2* and *s42p2* can be found in Figure 20 on the left. Thinner samples were not included due to RC limitations. This measurement indicates no change in mobility with the addition of the 5nm layer.

Following the previously outlined statistical procedure, the SCLC-Murgatroyd mobilities of all single-carrier devices, except for *s10p3* (overview in Figure 19) were processed and their interval plot can be found in Figure 20 on the right.

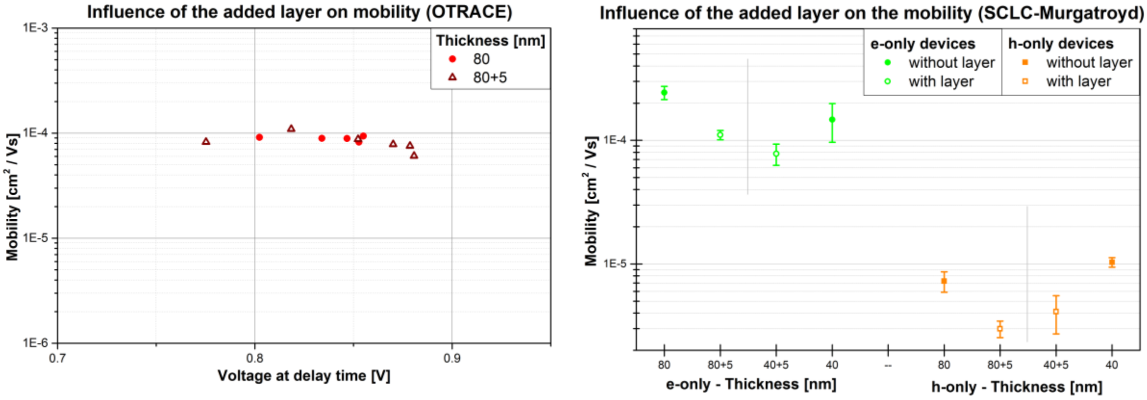

Figure 20 – On the left, OTRACE mobility measurements for *s12p2* (80 nm) and *s22p2* (80+5 nm). On the right, a statistical treatment of the SCLC-Murgatroyd mobilities of all single carrier devices except for *s10p3* (outlier). The error bars represent a 95% confidence interval for the mean value. For all samples N=8, with exception of the 80nm hole-only devices, where N=7.

SCLC mobilities for the added layer samples are slightly reduced in comparison to the samples without layer. This is not necessarily in contradiction with OTRACE, as this method takes into account ambipolar transport, as such, it is possible that the faster carrier is extracted sooner, leading to an overestimation of mobility. [51] The added layer must also be taken into account as it changes the contact interface, and it could affect the SCLC measurement differently.

Suns-V_{OC} - n_i

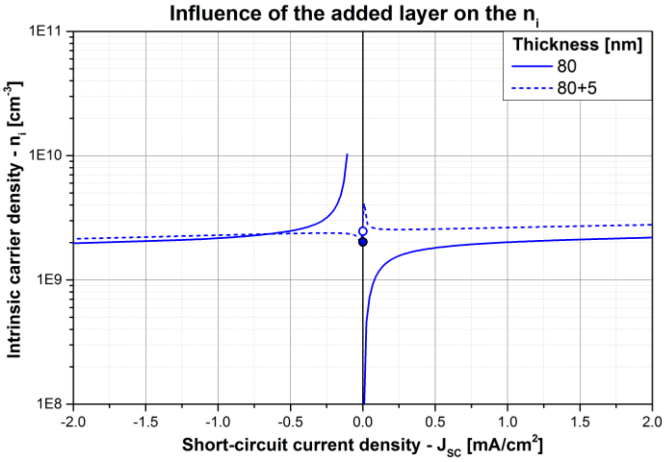

Figure 21 – Intrinsic carrier density plot of *s12p4* (80 nm) and *s22p4* (80+5 nm). Dashed and solid lines represent samples with and without layer respectively.

In Figure 21, the intrinsic carrier density plot for *s12p4* and *s22p4* can be observed. The plot suggests identical values for both samples. Table 5 presents a summary of the mobilities, recombination constant and the intrinsic carrier density.

Table 5 – Summary of the mean value of the effective mobility from SCLC (Murgatroyd model), mobility and recombination constant from OTRACE (*s12p2* and *s22p2*), as well as intrinsic carrier density from Suns-V_{OC}, for *s12p4* (80 nm) and *s22p4* (80+5 nm).

L [nm]	Mean μ_{eff} – SCLC (Mt) [cm^2/Vs]	µ-OTRACE [cm^2/Vs]	k_r [cm^3/µs]	n_i [cm^{-3}]
80	$4 \cdot 10^{-5}$	$9 \cdot 10^{-5}$	$3 \cdot 10^{-12}$	$2 \cdot 10^{9}$
80+5	$2 \cdot 10^{-5}$	$8 \cdot 10^{-5}$	$4 \cdot 10^{-12}$	$2 \cdot 10^{9}$

Simulation

Parameters from Table 5 and Table 4 were taken into account, *s12p4* and *s22p4* were simulated as represented in Figure 22. Both simulations present reasonable fits, with some overestimation of mobility in both cases, particularly in the 80+5 nm sample.

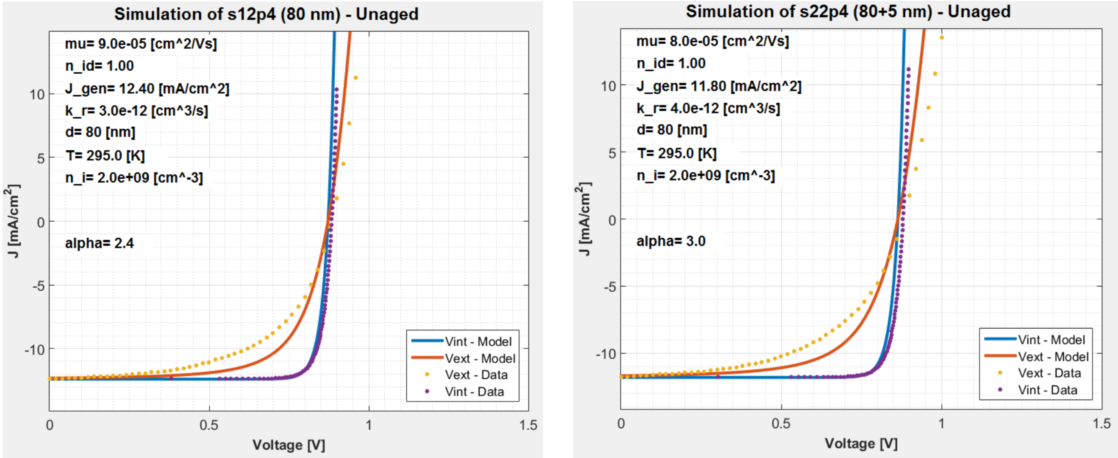

Figure 22 – Simulation of *s12p4* (80 nm) and *s22p4* (80+5 nm) on the left and right sides respectively. Solid lines indicate a simulation based on the parameters, and dotted lines indicate experimental data.

Summary

- In this run the addition of a 5nm protective layer caused no discernible change in the J_{SC} of all samples, as supported by EQE and JV measurements.

- No change was also observed in the V_{OC} according to the JV curves. Both the ideality factor from Suns-$\mathrm{V_{OC}}$ and the charge carrier lifetimes from TPV remained unchanged after degradation, thus supporting a constant V_{OC}.

- JV measurements revealed that the addition of the layer can cause a reduction in the average *FF* of up to approximately 8% for the 80 nm samples. Regarding the 40 nm samples the same cannot be concluded due their large variabilities, although it should be expected. While OTRACE measurements indicated no change in mobility, SCLC indicated a slight reduction in the mobility of samples with the layer. This disagreement may be due to an earlier extraction of faster carriers, thus leading to an overestimation in the OTRACE mobility. A change in the contact interface due to the extra layer is also a possibility for a difference in the SCLC measurement. Simulations revealed reasonable fits and overestimated mobilities for both unaged s12p4 (80 nm) and s22p4 (80+5 nm).

- The addition of the protective layer caused a reduction in the average *PCE* of up to approximately 1,3%. This was mostly due to a slight reduction in *FF*, itself due to a slight reduction in mobility.

3.2.1 Degradation of the second run

Half of the second run was degraded in identical conditions to the first one, i.e. inside an oven at 85 ºC for 1000h in the dark, thus leaving only the replica samples in pristine condition. A reduction in device characteristic parameters was expected, with exception of layer protected samples, which should present slower degradation.

External Quantum Efficiency

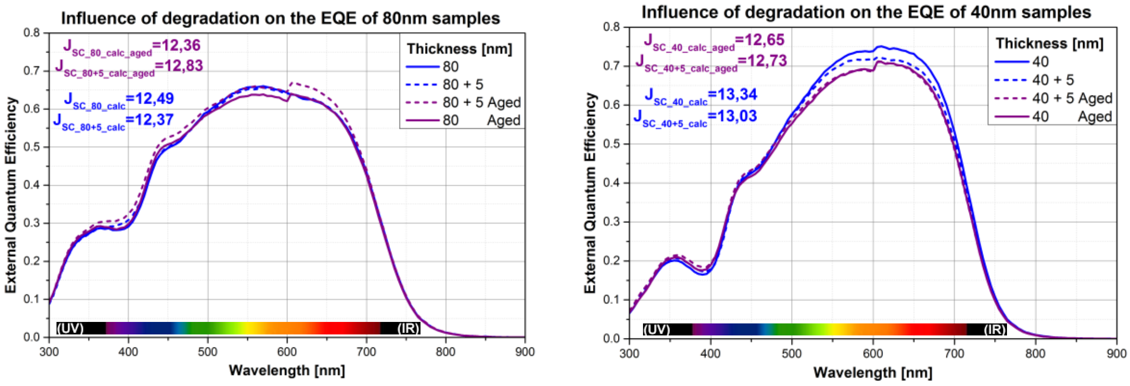

Figure 23 – EQE curves of *s12p4* (80 nm), *s22p4* (80 + 5 nm), *s32p4* (40 + 5 nm) and *s42p4* (40 nm) before (blue) and after (purple) degradation. Dashed and solid lines represent samples with and without layer respectively.

The EQE spectra of *s12p4* (80 nm), *s22p4* (80 + 5 nm), *s32p4* (40 + 5 nm) and *s42p4* (40 nm) before and after degradation can be found in Figure 23. The EQE spectra of the 80 nm samples seem to indicate no change. For the 40 nm samples however, there seems to be a slight decrease in the EQE spectra. This seemingly contradictory result may be explained by non-linear scaling of the photocurrent at low light intensities. Because of this, a white bias light is needed, particularly for degraded samples. [52]

Characteristic Curves

The JV curves of *s12p4***,** *s22p4*, *s32p4* and *s42p4* can be found in Figure 25. The curves show a reduction of *FF* and J_{SC} after degradation of the unprotected samples. The added layer seems to reduce this effect. A reduction of V_{OC} is also visible for all samples.

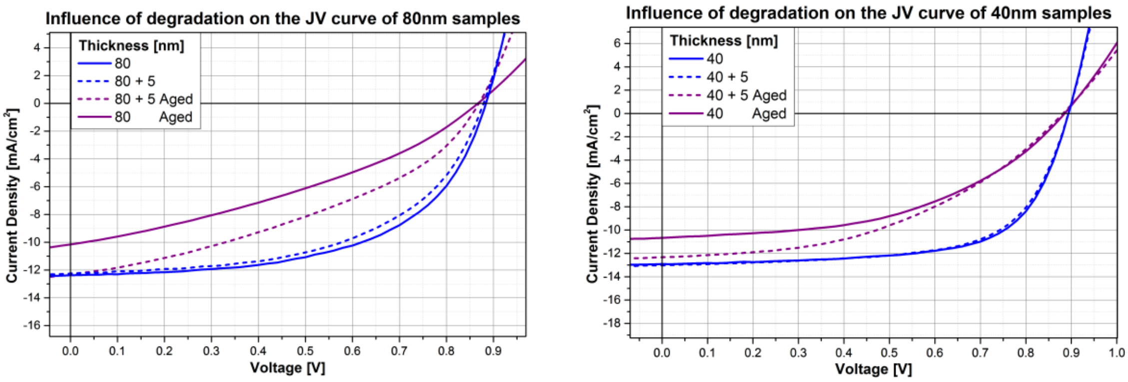

Figure 25 – Characteristic curves of *s12p4* (80 nm), *s22p4* (80 + 5 nm), *s32p4* (40 + 5 nm) and *s42p4* (40 nm) before (blue) and after (purple) degradation.

By following the previously outlined statistical procedures, interval plots for the performance characteristics (J_{SC}, V_{OC}, *FF* and *PCE*) of all degraded OSCs, with exception of *s22p1* and *s32p3*, were made and can be found in Figure 28. A more clear overview of these samples is presented in Figure 24.

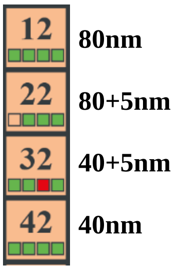

Figure 24 – Sample overview

Firstly, larger variabilities can be seen for the 40 nm samples. The average J_{SC} of the 80+5* nm samples clearly suffered less degradation when compared to the 80* nm samples. The same cannot be said of the 40+5* nm samples, whose large variabilities make comparisons more difficult, although the average value is slightly higher and some preservation could have occurred. It is possible that the different optical interference patterns caused by different thicknesses, may compromise the effectiveness of the protective layer. Regarding the *FF*, for 80+5* nm samples a maximum of ≈12% in the average *FF* was conserved after degradation, when compared with the 80 nm samples. V_{OC} seems to have lowered slightly for all samples (few tens of mV) with no effect from the layer. The unaged measurements were performed in a warmer environment than the aged ones, as such, this reduction in V_{OC} can not be attributed to a difference in temperature, furthermore, this implies that the reduction in V_{OC} is underestimated. The *PCE* reflects these effects, particularly the slower J_{SC} degradation. After 1000h of degradation, a maximum of ≈3,8% of the average *PCE* was conserved by this layer when comparing the 80+5* nm to 80* nm degraded samples.

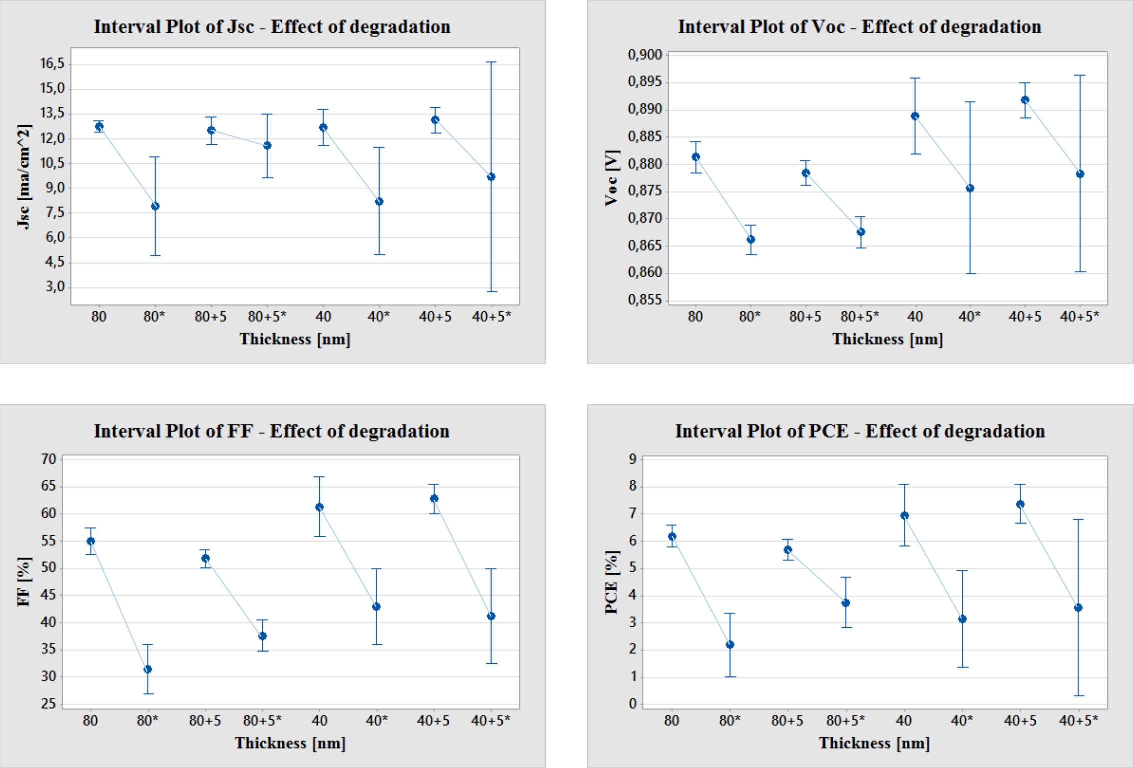

Figure 26 – Interval plots of the performance characteristics of all degraded samples with exception of *s22p1* and *s32p3*. Vertical bars represent a 95% confidence interval for the mean value. Degraded samples are marked with *. The light blue lines connecting pristine to degraded samples are exclusively used as a visual aid, their slopes can be compared to each other to estimate how differently degradation affected each sample.

Suns-V_{OC}

The ideality factor characterization of *s12p4*, *s22p4*, *s32p4* and *s42p4* can be found in Figure 27. Recalling Eq. (1.11), and as observed in this characterization, there is no

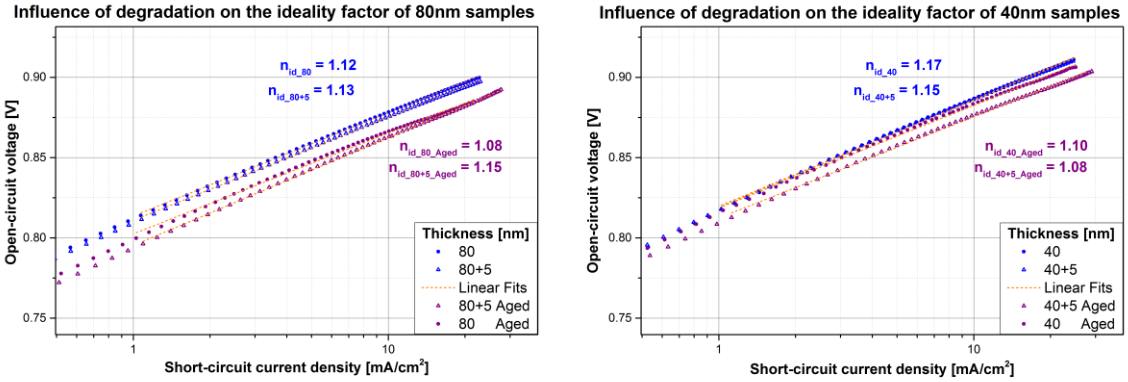

Figure 27 – Ideality factor characterization of *s12p4* (80 nm), *s22p4* (80+5 nm), *s32p4* (40+5 nm) and *s42p4* (40 nm), before (blue) and after degradation (purple).

change in n_{id}, thus there appears to be no change in the recombination mechanism after degradation.

Transient Photovoltage

The charge carrier lifetime characterization for the same samples can be found in Figure 28. The lifetime plots suggest an increase in charge carrier lifetime.

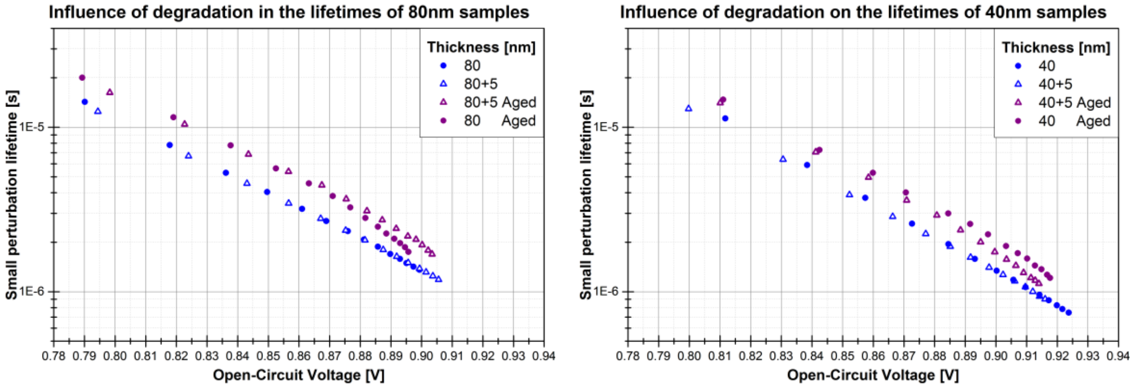

Figure 28 – Charge carrier lifetime characterization of *s12p4* (80 nm), *s22p4* (80+5 nm), *s32p4* (40+5 nm) and *s42p4* (40 nm), before (blue) and after degradation (purple).

Taking into account the reduced V_{OC} obtained by the JV curve, and that this reduction was not due to temperature, an increase in recombination is implied. Since n_{id} has not changed, the recombination mechanism is identical. Assuming that a broadening of the density of states (DOS) has occurred, this would lead to a decrease in V_{OC}, and increased trapping of charge carriers, thus delaying recombination and increasing lifetime as well as reducing mobility.

OTRACE and SCLC

The OTRACE mobility measurements for *s12p2* and *s22p2* before and after degradation can be found in Figure 30 on the left. Samples of lower thickness were not included due to RC limitations. The OTRACE technique suggests no significant change in mobility, which isn't necessarily contradictory to a small decrease in mobility, as OTRACE could have extracted the faster carriers, thus leading to an overestimation of mobility.

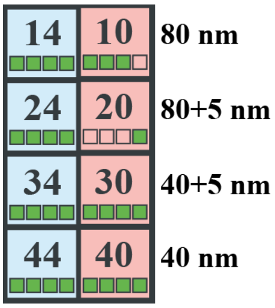

Figure 29 – Sample overview

The previously outlined statistical procedure was followed, with exception for outlier exclusions. Interval plots for the SCLC-Murgatroyd mobility can be found in Figure 30 on the right. An overview of the samples used in the statistical treatment is located in Figure 29. Unsuccessful fits are represented with no color; Only half of the run was degraded, thus the available number of samples for this analysis is halved, and unsuccessful fits or outlier values can further reduce this number, therefore variabilities of these parameters are expected to increase in comparison to their unaged counterparts.

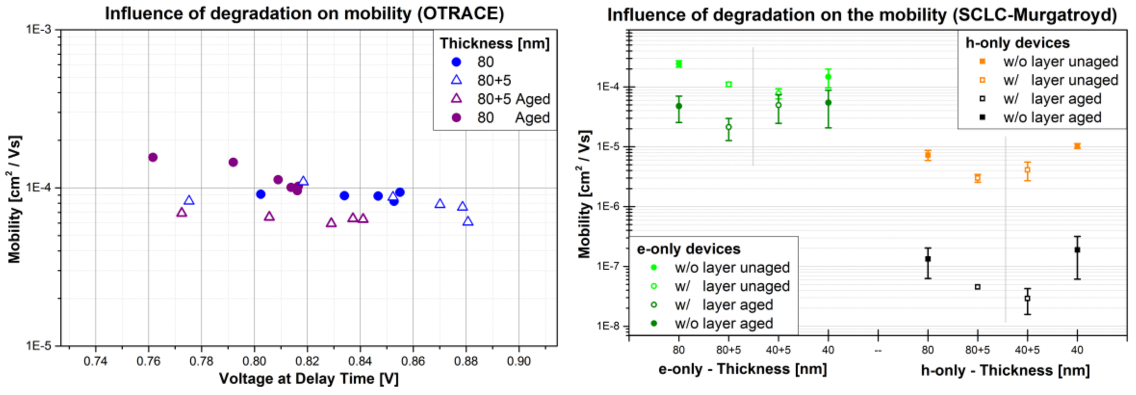

Figure 30 – On the left, OTRACE mobility measurements for *s12p2* (80 nm) and *s22p2* (80+5 nm) before and after degradation. On the right, SCLC for the electron and hole mobilites.

The SCLC mobility measurements suggest a reduction in electron mobility for all samples, particulary for the 80 and 80+5 nm, and a decrease of approximately two orders of magnitude in the hole mobility of all samples. Such a large decrease is indicative of problems with the injection of charges due to degradation, particularly for hole-only devices, additionally the number of failed fits is higher for these devices, further supporting that SCLC is prone to contact problems and that fittings are troublesome for very low mobility values.

Suns-V_{OC} - n_i

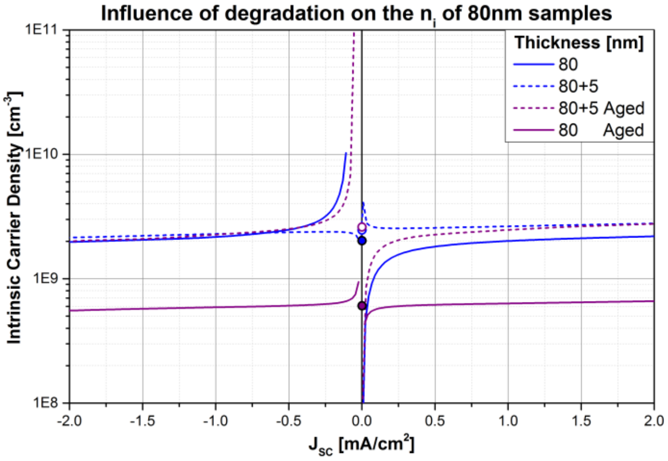

Figure 31 – Intrinsic carrier density plot of *s12p4* (80 nm) and *s22p4* (80+5 nm) before (blue) and after degradation (purple). Dashed and solid lines represent samples with and without layer respectively.

In Figure 31 the intrinsic carrier density plot of *s12p4* and *s22p4* can be observed. This measurement indicates a single value of n_i for all samples with exception of *s22p4* (80 nm) which presents a lower value, by approximately half. Table 6 presents a summary of the mobilities, recombination constant and intrinsic carrier density measurements.

Table 6 – Summary of the mean value of the effective mobility from SCLC (Murgatroyd model), mobility and recombination constant from OTRACE, as well as intrinsic carrier density from Suns-V_{OC}, for s12p4 (80nm) and s22p4(80+5nm) before and after degradation.

L [nm]	**Condition**	**$\mu_{eff\text{-}avg}$ – SCLC (Mt) [cm^2/Vs]**	**μ-OTRACE [cm^2/Vs]**	**k_r [$cm^3/\mu s$]**	**n_i [cm^{-3}]**
80	Pristine	$4\cdot10^{-5}$	$9\cdot10^{-5}$	$3\cdot10^{-12}$	$2\cdot10^{9}$
	Aged	$4\cdot10^{-6}$	$1\cdot10^{-4}$	$2\cdot10^{-12}$	$6\cdot10^{8}$
80+5	Pristine	$2\cdot10^{-5}$	$8\cdot10^{-5}$	$4\cdot10^{-12}$	$2\cdot10^{9}$
	Aged	$1\cdot10^{-6}$	$6\cdot10^{-5}$	$2\cdot10^{-12}$	$2\cdot10^{9}$

Simulation

The model parameters can be observed next to the simulations, in Figure 32. By looking at the internal voltage curves, free of parasitic effects, a clear underestimation of n_i can be observed for *s12p4*, which due to the model of the n_i measurement, suggests an overestimation of mobility has occurred. More specifically, if the ni value of *s12p4* ($6\cdot10^{8}$cm^{-3}) were to be doubled, its mobility ($1\cdot10^{-4}$cm^2/Vs) would be halved, thus values of $1,2\cdot10^{9}$cm^{-3}and $5\cdot10^{-5}$cm^2/Vs would be obtained respectively. As such, a small reduction in mobility is possible but remains to be verified.

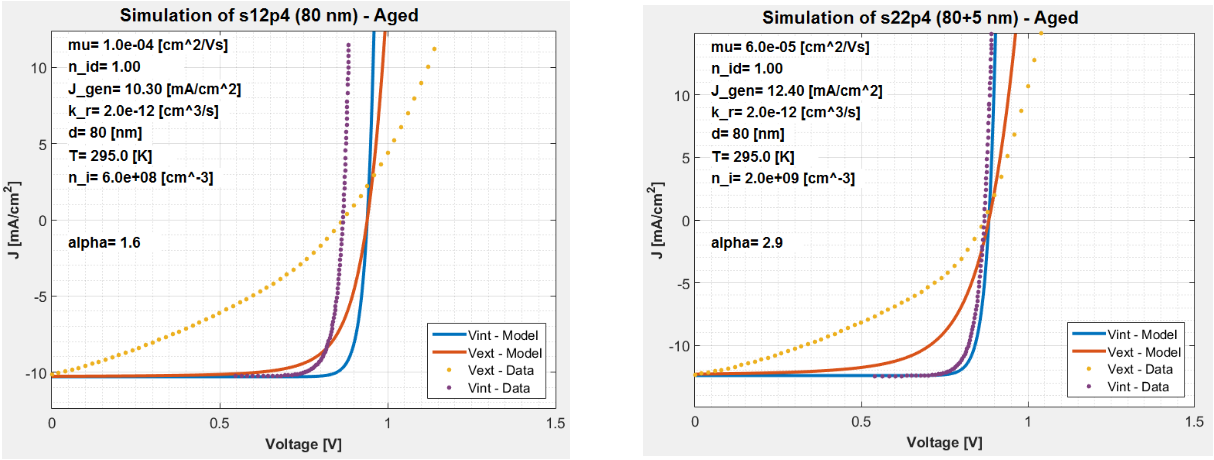

Figure 32 – Simulation of unaged *s12p4* (80 nm) and *s22p4* (80+5 nm) on the left and right sides respectively. Solid lines indicate the simulation based on shown parameters, and dotted lines indicate experimental data.

Summary

- In this run, with high temperature degradation for 1000h in darkness, the 5nm added layer was able to considerably slow down the degradation of the average J_{SC} for the 80+5nm samples (reduced by up to 3mA) when compared to the unprotected ones (reduced by up to 8mA). The thinnest samples had large variabilities and although they may suggest some protection of the layered samples, a statistical study with higher sampling would be required for a more solid conclusion. The disagreement between JV curves and EQE spectra can be attributed to the requirement of using a white bias light for the latter, in the case of degraded OSCs.

- A reduction in the V_{OC} of all samples was observed, according to the JV curves. The ideality factor from Suns-V_{OC} remained unchanged, implying also no change in the recombination mechanism. However, charge carrier lifetimes from TPV indicated an increase upon ageing. This could be explained by a broadening of the density of states, however a decrease in mobility is to be expected. To further investigate this hypothesis impedance spectroscopy measurements [56] or thermally stimulated current measurements (TSC) [54,55] would be used.

- JV curves determined a reduction in *FF* for all samples, however, for the 80+5 nm samples the layer was able to conserve up to ≈12% of the average *FF* in comparison with the 80 nm samples. OTRACE indicated no change in mobility. In stark contrast, SCLC indicated a reduction of approximately two orders of magnitude in hole mobility and a smaller reduction in electron mobility. This could have been due bad contacts caused by degradation, particularly for hole-only devices. Simulations revealed an agreeable fit for s22p4 (80+5 nm) but not for s21p4 (80nm) which indicated an underestimation of n_i by a factor of 0,5 and thus implied an overestimation of mobility by a factor of 2.

- Comparing the 80nm with the 80+5nm samples, a protection of up to ≈3,8% in the average *PCE* was obtained. The added layer may cause an initial reduction in the *PCE*, however, it is able to slow down degradation, thus making it a useful addition where high longevity is required in an OSC.

4 Conclusions and Future Perspectives

In this thesis the effect of degradation on the charge transport and recombination dynamics of photo-generated charges in organic photovoltaic devices was investigated. An understanding of the relationship between characteristic device parameters and material properties was developed.

The degradation (85ºC in darkness for 1000h) of OSCs, made with proprietary materials from Heliatek GmbH was studied through the use of basic techniques (EQE, JV) were used to obtain characteristic device parameters (J_{SC}, V_{OC}, *FF*, *PCE*), as well as Suns-V_{OC} (n_{id} and n_i) and TPV (τ – charge carrier lifetime) regarding recombination. OTRACE (μ), a novel technique to measure mobility, was used, as well as SCLC (μ_e and μ_h) with the Murgatroyd and Mott-Gurney models, of which the former was mostly used. Simulations were performed based on the model by Neher [36]. Given such a high temperature for degradation (85ºC), it is possible that the device reached or even surpassed the glass transition temperature of the HTL material, which would result in a loss of its conductivity and in diffusion of dopants to the subsequent layer. [57]

Results of the first run indicate a reduction in *PCE,* mostly due to a reduction in *FF,* itself due to extrinsic factors such as parasitic resistances. No difference in degradation was noted between the good batch and bad batch materials. In an attempt to slow down degradation a 5nm protective layer was used in the second run. Results indicated that the layer caused a reduction of up to 1,3% of average *PCE,* which was due mostly to a reduction in *FF,* itself due to a slight reduction in mobility. Upon degradation of the second run, results indicated a decrease in all parameters for all samples, although with slower reduction of *FF* and a much more pronounced, slower reduction of J_{SC} for the 80+5 nm samples. Thus the added layer was able to preserve up to ≈3,8% of average *PCE* for these samples.

4.1 Future Perspectives

Additional measurements can be performed to obtain more information about the samples studied in this thesis. Since there was a reduction in V_{OC} for degradation of the last run, it would be interesting to perform a sensitive EQE measurement [53], which reveals information on the CT state energy and recombination losses. Measurement of EQE with a white bias light can reveal a reduction in the EQE spectrum for samples with more advanced degradation [52].

For further understanding of recombination mechanisms, methods such as transient absorption spectroscopy (TAS) could be used, since this is an optical method it will not subjected to electrical effects such as RC limitations or extraction losses. [39]

Regarding the previously stated hypothesis, that a broadening of the DOS would be responsible for an increase in charge carrier lifetime, techniques such as thermally stimulated current (TSC) [54,55] for trap state measurements, or impedance spectroscopy [56] for carrier lifetime and DOS measurements, could be used to determine its validity.

Currently, there is no standard mobility measurement, thus a comparison of a select group, among the several available methods such as, POEM [19], TOF, OTRACE [42,43], SCLC and other variants, would be relevant in determining their effectiveness and validity over a range of materials, or parameters, such as conductivity.

A protective layer capable of slowing degradation would be greatly beneficial in improving OSC longevity. As such, investigating possible connections between the protective effect of the layer and other variables, such as thickness, would be relevant. Measurements of the surface roughness of this layer would also be relevant in understanding how to optimize the protection effect of the layer, while minimizing its initial negative impact on OSC performance.

References

[1] R.E.P.N. for the 21st Century (REN21), *Renewables 2016 - Global Status Report*, 2016.

[2] E. Comission, “A policy framework for climate and energy in the period from 2020 to 2030,” Jan. 2014.

[3] F.M. for Economic Affairs and Energy, “Renewable Energy Sources Act,” Aug. 2014.

[4] N.S. Lewis and D.G. Nocera, “Powering the planet: Chemical challenges in solar energy utilization,” *Proceedings of the National Academy of Sciences*, vol. 103, 2006, pp. 15729–15735.

[5] N.R.E.L. (NREL), “Best Research-Cell Efficiencies,” 2016.

[6] C.J. Brabec, “Organic photovoltaics: technology and market,” *Solar energy materials and solar cells*, vol. 83, 2004, pp. 273–292.

[7] C.W. Tang, “Two-layer organic photovoltaic cell,” *Applied Physics Letters*, vol. 48, 1986.

[8] H. GmbH, *Heliatek sets new Organic Photovoltaic world record efficiency of 13.2%*, 2016.

[9] Heliatek, “Pilot Projects,” 2016.

[10] W. Tress, *Organic Solar Cells - Theory, Experiment, and Device Simulation*, Springer, 2014.

[11] J. Zhao, Y. Li, G. Yang, K. Jiang, H. Lin, H. Ade, W. Ma, and H. Yan, “Efficient organic solar cells processed from hydrocarbon solvents,” *Nature Energy*, vol. 1, 2016, p. 15027.

[12] K. Cnops, B.P. Rand, D. Cheyns, B. Verreet, M.A. Empl, and P. Heremans, “8.4% efficient fullerene-free organic solar cells exploiting long-range exciton energy transfer,” *Nature communications*, vol. 5, 2014.

[13] S. Albrecht, J.R. Tumbleston, S. Janietz, I. Dumsch, S. Allard, U. Scherf, H. Ade, and D. Neher, “Quantifying Charge Extraction in Organic Solar Cells: The Case of Fluorinated PCPDTBT,” *The Journal of Physical Chemistry Letters*, vol. 5, 2014, pp. 1131–1138.

[14] B. Ray and M.A. Alam, “Achieving Fill Factor Above 80% in Organic Solar Cells by Charged Interface,” *Journal of Photovoltaics*, 2012.

[15] M. Schwoerer and H.C. Wolf, *Organic molecular solids*, John Wiley & Sons, 2007.

[16] S.M. Sze, *Physics of Semiconductor Devices*, John Wiley & Sons, 1969.

[17] J. Cottaar, R. Coehoorn, and P. Bobbert, “Modeling of charge transport across disordered organic heterojunctions,” *Or*, vol. 13, 2012, pp. 667–672.

[18] V. Kažukauskas, A. Arlauskas, M. Pranaitis, R. Lessmann, M. Riede, and K. Leo, “Characterization of effective charge carrier mobility in ZnPc/C60 solar cells after ageing,” *physica status solidi (c)*, vol. 6, 2009, pp. 2864–2866.

[19] J. Widmer, J. Fischer, W. Tress, K. Leo, and M. Riede, “Electric potential mapping by thickness variation: A new method for model-free mobility determination in organic semiconductor thin films,” *Organic Electronics*, vol. 14, 2013, pp. 3460–3471.

[20] N.F. Mott and R.W. Gurney, “Electronic processes in ionic crystals,” 1940.

[21] P.N. Murgatroyd, “Theory of space-charge-limited current enhanced by Frenkel effect,” *Applied Physics*, vol. 3, 1970, pp. 151–156.

[22] W. Pasveer, J. Cottaar, C. Tanase, R. Coehoorn, P. Bobbert, P. Blom, D. De Leeuw, and M. Michels, “Unified description of charge-carrier mobilities in disordered semiconducting polymers,” *Physical review letters*, vol. 94, 2005, p. 206601.

[23] K. Vandewal, “Interfacial Charge Transfer States in Condensed Phase Systems,” *Annual review of physical chemistry*, vol. 67, 2016, pp. 113–133.

[24] R.R. Lunt, N.C. Giebink, A.A. Belak, J.B. Benziger, and S.R. Forrest, “Exciton diffusion lengths of organic semiconductor thin films measured by spectrally resolved photoluminescence quenching,” *Journal of Applied Physics*, vol. 105, 2009.

[25] T.M. Clarke and J.R. Durrant, “Charge Photogeneration in Organic Solar Cells,” *Chemical Reviews*, vol. 110, 2010, pp. 6736–6767.

[26] D. Wynands, B. Maennig, M. Riede, K. Leo, E. Brier, E. Reinold, and P. Baeuerle, “Organic thin film photovoltaic cells based on planar and mixed heterojunctions between fullerene and a low bandgap oligothiophene,” *Journ*, vol. 106, 2009.

[27] A. De Vos, “Detailed balance limit of the efficiency of tandem solar cells,” *Journal of Physics D: Applied Physics*, vol. 13, 1979, pp. 839–846.

[28] C.W. Schlenker, V.S. Barlier, S.W. Chin, M.T. Whited, R.E. McAnally, S.R. Forrest, and M.E. Thompson, “Cascade Organic Solar Cells,” *Chemistry of Materials*, vol. 23, 2011, pp. 4132–4140.

[29] P. Wuerfel, “Physics of Solar Cells,” 2005.

[30] H. Hoppe, N. Arnold, D. Meissner, and N.S. Sariciftci, “Modeling of optical absorption in conjugated polymer/fullerene bulk-heterojunction plastic solar cells,” *Thin Solid Films,* vol. 451, 2004, pp. 589–592.

[31] B. Maennig, J. Drechsel, D. Gebeyehu, P. Simon, F. Kozlowski, A. Werner, F. Li, S. Grundmann, S. Sonntag, M. Koch, K. Leo, M. Pfeiffer, H. Hoppe, D. Meissner, N.S. Sariciftci, I. Riedel, V. Dyakonov, and J. Parisi, “Organic p-i-n solar cells,” *Applied Physics A,* vol. 79, 2004, pp. 1–14.

[32] D. Nanova, M. Scherer, F. Schell, J. Zimmermann, T. Glaser, A.K. Kast, C. Krekeler, A. Pucci, W. Kowalsky, R.R. Schröder, and others, “Why Inverted Small Molecule Solar Cells Outperform Their Noninverted Counterparts,” *Advanced Functional Materials*, vol. 25, 2015, pp. 6511–6518.

[33] U. Wuerfel, D. Neher, A. Spies, and S. Albrecht, “Impact of charge transport on current-voltage characteristics and power-conversion efficiency of organic solar cells,” *Nature communications,* 2015.

[34] W. Tress, S. Corvers, K. Leo, and M. Riede, “Investigation of Driving Forces for Charge Extraction in Organic Solar Cells - Transient Photocurrent Measurements on Solar Cells Showing S-Shaped Current–Voltage Characteristics,” *Advanced Energy Materials,* 2013.

[35] W. Tress, K. Leo, and M. Riede, “Influence of Hole-Transport Layers and Donor Materials on Open-Circuit Voltage and Shape of I–V Curves of Organic Solar Cells,” *Advanced Functional Materials,* vol. 21, 2011, pp. 2140–2149.

[36] D. Neher, J. Kniepert, A. Elimelech, and L.J.A. Koster, “A New Figure of Merit for Organic Solar Cells with Transport-limited Photocurrents,” *Scientific reports,* vol. 6, 2016.

[37] V. Shrotriya, G. Li, Y. Yao, T. Moriarty, K. Emery, and Y. Yang, “Accurate measurement and characterization of organic solar cells,” *Advanced Functional Materials,* vol. 16, 2006, pp. 2016–2023.

[38] N.R.E.L. (NREL), “Device Performance - Measurements & Characterization,” Jul. 2006.

[39] T.M. Clarke, C. Lungenschmied, J. Peet, N. Drolet, and A.J. Mozer, “A Comparison of Five Experimental Techniques to Measure Charge Carrier Lifetime in Polymer/Fullerene Solar Cells,” *Advanced Energy Materials,* vol. 5, 2015.

[40] E. Nakane, K. Kaneko, T. Mori, T. Mizutani, H. Takino, and M. Ishioka, “Effects of electrodes on space charge in polypropylene,” *CEIDP’05. 2005 Annual Report Conference on Electrical Insulation and Dielectric Phenomena, 2005.*, IEEE, 2005, pp. 653–656.

[41] A.J. Mozer, D. Dennler, N.S. Sariciftci, M. Westerling, and A. Pivrikas, “Time-dependent mobility and recombination of the photoinducted charge carriers in conjugated polymer/fullerene bulk heterojunction solar cells,” *Faculty of Science, Medicine and Health - Papers,* vol. 72, 2005.

[42] A. Baumann, J. Lorrman, C. Deibel, and V. Dyakonov, “A New Approach for Probing the Mobility and Lifetime of Photogenerated Charge Carriers in Organic

Solar Cells Under Real Operating Conditions," *Advanced Materials*, vol. 24, 2012, pp. 4381–4386.

[43] J. Lorrmann, B.H. Badada, O. Inganäs, V. Dyakonov, and C. Deibel, "Charge carrier extraction by linearly increasing voltage: Analytic framework and ambipolar transients," *Journal of Applied Physics*, vol. 108, 2010, p. 113705.

[44] R. Sinton, A. Cuevas, and others, "A quasi-steady-state open-circuit voltage method for solar cell characterization," *Proceedings of the 16th European Photovoltaic Solar Energy Conference*, 2000.

[45] S. Schiefer, B. Zimmermann, S.W. Glunz, and U. Wuerfel, "Applicability of the Suns-VOC Method on Organic Solar Cells," *Journal of Photovoltaics*, vol. 4, 2014, pp. 271–277.

[46] M.J. Kerr, A. Cuevas, and R.A. Sinton, "Generalized analysis of quasi-steady-state and transient decay open circuit voltage measurements," *Journal of applied physics*, vol. 91, 2002, pp. 399–404.

[47] S. Schiefer, B. Zimmermann, and U. Wuerfel, "Determination of the intrinsic and the injection dependent charge carrier density in organic solar cells using the Suns-VOC method," *Journal of Applied Physics*, vol. 115, 2014.

[48] M. Wolf and H. Rauschenbach, "Series resistance effects on solar cell measurements," *Advanced energy conversion*, vol. 3, 1963, pp. 455–479.

[49] S.M. Ross, "Peirce's criterion for the elimination of suspect experimental data," *Journal of Engineering Technology*, 2003.

[50] J.C. de Winter, "Using the Student's t-test with extremely small sample sizes," *Practical Assessment, Research & Evaluation*, vol. 18, 2013, pp. 1–12.

[51] L. Koster, V. Mihailetchi, and P. Blom, "Bimolecular recombination in polymer/fullerene bulk heterojunction solar cells," *Applied physics letters*, vol. 88, 2006, p. 052104.

[52] M. Hermenau, "Lebensdaueruntersuchungen an organischen Solarzellen," 2012.

[53] J. Benduhn, "Sensitive Spectroscopy of Charge-Transfer States and Triplet Excited States in Organic Photovoltaics," Institut für Angewandte Photophysik - Fachrichtung Physik Fakultät für Mathematik und Naturwissenschaften - Technische Universität Dresden, 2015.

[54] R.R. Haering and E.N. Adams, "Theory and application of thermally stimulated currents in photoconductors," *Physical Review*, vol. 117, 1960, p. 451.

[55] V. Kažukauskas, M. Pranaitis, F. Kajzar, M. Glatthaar, and A. Hinsch, "Charge carrier trapping in organic solar cell structures P3HT: PCBM," *Molecular Crystals and Liquid Crystals*, vol. 484, 2008, pp. 373–739.

[56] G. Garcia-Belmonte, P.P. Boix, J. Bisquert, M. Sessolo, and H.J. Bolink, "Simultaneous determination of carrier lifetime and electron density-of-states in P3HT: PCBM organic solar cells under illumination by impedance spectroscopy," *Solar Energy Materials and Solar Cells*, vol. 94, 2010, pp. 366–375.

[57] F.C. Krebs, *Stability and degradation of organic and polymer solar cells*, Wiley Online Library, 2012.

Annex

Annex A – Physical Constants

Description	Value
Speed of light in vacuum – c	$2.99792 \cdot 10^{8}$ [m/s]
Elementary charge – q	$1.60218 \cdot 10^{-19}$ [As]
Planck's constant – h	$6.60627 \cdot 10^{-34}$ [Js]
Boltzmann's constant – k_B	$1.38065 \cdot 10^{23}$ [J/K]
Vaccuum permitivity – ϵ_0	$8.85419 \cdot 10^{-12}$ [$A^2 s^4 (kg\ m^3)^{-1}$]

Annex B – Acronyms

PV	Photovoltaic
OPV	Organic Photovoltaic
BIPV	Building Integrated Photovoltaic
PCE	Power Conversion Efficiency
FF	Fill Factor
OSC	Organic Solar Cell
HOMO	Highest Occupied Molecular Orbit
LUMO	Lowest Unoccupied Molecular Orbit
DA	Donor-Acceptor
CT	Charge-Transfer
FHJ	Flat Heterojunction
BHJ	Bulk Heterojunction
PMHJ	Planar-Mixed Heterojunction
HTL	Hole Transport Layer
ETL	Electron Transport Layer
ITO	Indium-Tin-Oxide
EQE	External Quantum Efficiency

SRC	Standard Reporting Conditions
SMU	Source Measuring Unit
MM	Mismatch Factor
Mt	Murgatroyd
MG	Mott-Gurney
TPV	Transient Photovoltage
OC	Open-Circuit
LED	Light Emitting Diode
PSU	Power Supply Unit
SCLC	Space Charge Limited Current
OTRACE	Open-Circuit Corrected Charge Carrier Extraction
CELIV	Charge Extraction by Linearly Increasing Voltage
POEM	Electric Potential Mapping by Thickness Variation

Annex C – Pixel Areas

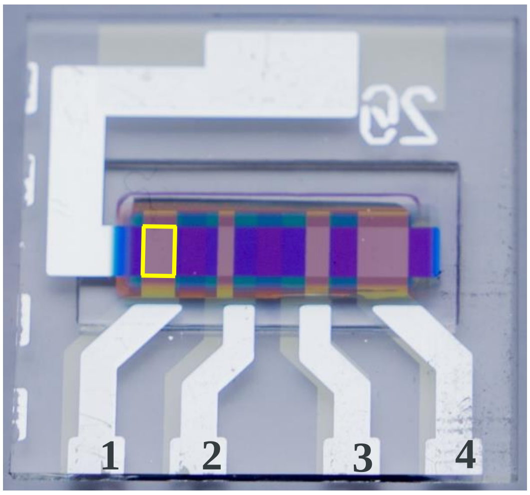

p4: 2.540 x 2.540 [mm] + 0.09 mm^2 = **6.440 mm^2**

p3: 1.270 x 2.540 [mm] + 0.09 mm^2 = **3.316 mm^2**

p2: 0.898 x 2.540 [mm] + 0.09 mm^2 = **2.371 mm^2**

p1: 1.796 x 2.540 [mm] + 0.09 mm^2 = **4.652 mm^2**

Annex D – Heliatek 1st run planning sheet

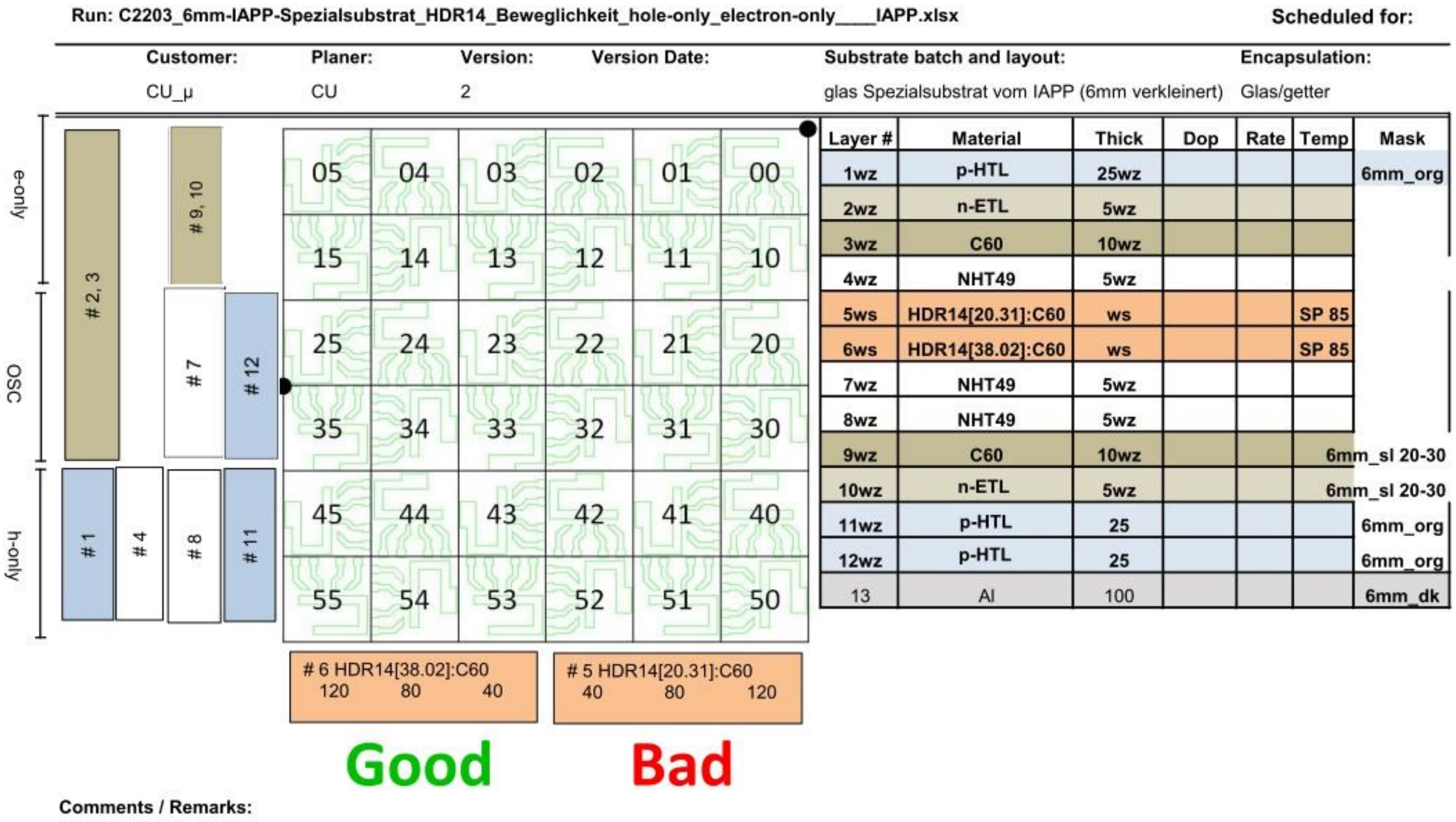

Run: C2203_6mm-IAPP-Spezialsubstrat_HDR14_Beweglichkeit_hole-only_electron-only____IAPP.xlsx **Scheduled for:**

Customer:	Planer:	Version:	Version Date:	Substrate batch and layout:	Encapsulation:
CU_µ	CU	2		glas Spezialsubstrat vom IAPP (6mm verkleinert)	Glas/getter

Layer #	Material	Thick	Dop	Rate	Temp	Mask
1wz	p-HTL	25wz				6mm_org
2wz	n-ETL	5wz				
3wz	C60	10wz				
4wz	NHT49	5wz				
5ws	HDR14[20.31]:C60	ws			SP 85	
6ws	HDR14[38.02]:C60	ws			SP 85	
7wz	NHT49	5wz				
8wz	NHT49	5wz				
9wz	C60	10wz				6mm_sl 20-30
10wz	n-ETL	5wz				6mm_sl 20-30
11wz	p-HTL	25				6mm_org
12wz	p-HTL	25				6mm_org
13	Al	100				6mm_dk

05	04	03	02	01	00
15	14	13	12	11	10
25	24	23	22	21	20
35	34	33	32	31	30
45	44	43	42	41	40
55	54	53	52	51	50

6 HDR14[38.02]:C60
120 80 40

5 HDR14[20.31]:C60
40 80 120

Good **Bad**

Comments / Remarks:

Annex E - Heliatek 2nd run planning sheet

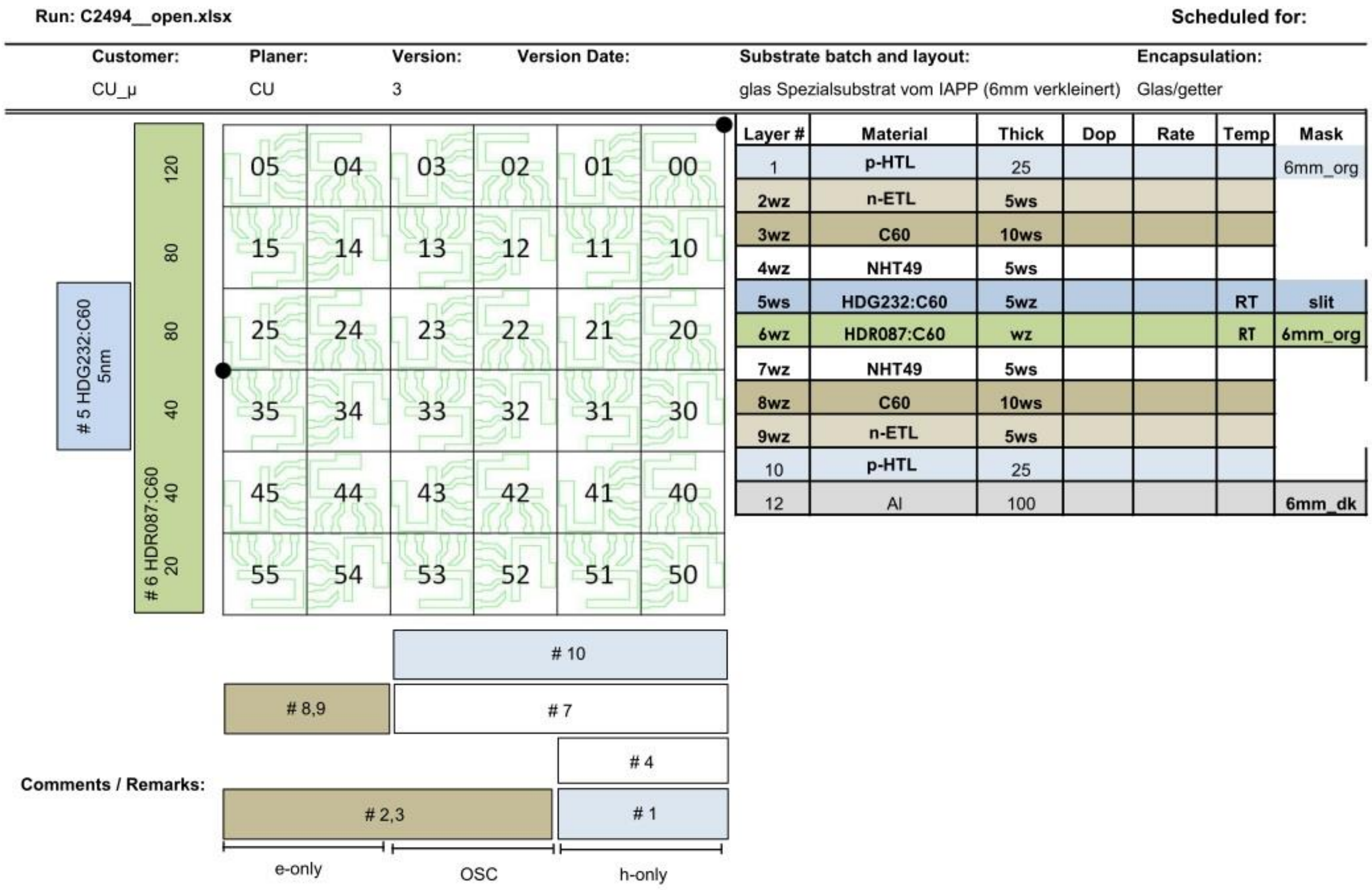

Run: C2494__open.xlsx **Scheduled for:**

Customer:	**Planer:**	**Version:**	**Version Date:**	**Substrate batch and layout:**	**Encapsulation:**
CU_µ	CU	3		glas Spezialsubstrat vom IAPP (6mm verkleinert)	Glas/getter

Layer #	Material	Thick	Dop	Rate	Temp	Mask
1	p-HTL	25				6mm_org
2wz	n-ETL	5ws				
3wz	C60	10ws				
4wz	NHT49	5ws				
5ws	HDG232:C60	5wz			RT	slit
6wz	HDR087:C60	wz			RT	6mm_org
7wz	NHT49	5ws				
8wz	C60	10ws				
9wz	n-ETL	5ws				
10	p-HTL	25				
12	Al	100				6mm_dk

05	04	03	02	01	00
15	14	13	12	11	10
25	24	23	22	21	20
35	34	33	32	31	30
45	44	43	42	41	40
55	54	53	52	51	50

Comments / Remarks:

Annex F – SCLC models

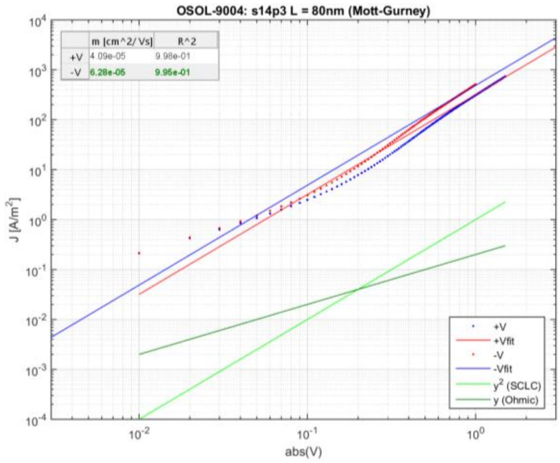

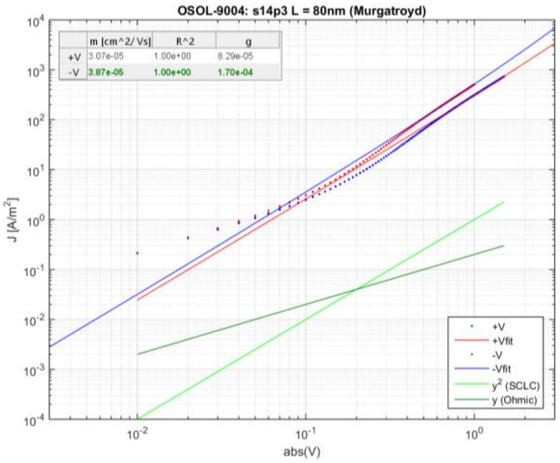

In this case the single carrier device presents ohmic contacts (data points parallel to dark green line for low voltages) and for higher voltages the device reaches SCLC (data points parallel to light green line) with very little field dependence ($\gamma = 2\cdot10^{-4}\ \sqrt{cm/V}$), thus both models (solid lines) are adequate for fitting and present similar values, $6\cdot10^{-5}$ cm^2/Vs for the Mott-Gurney model and $4\cdot10^{-5}$ cm^2/Vs for the Murgatroyd model.

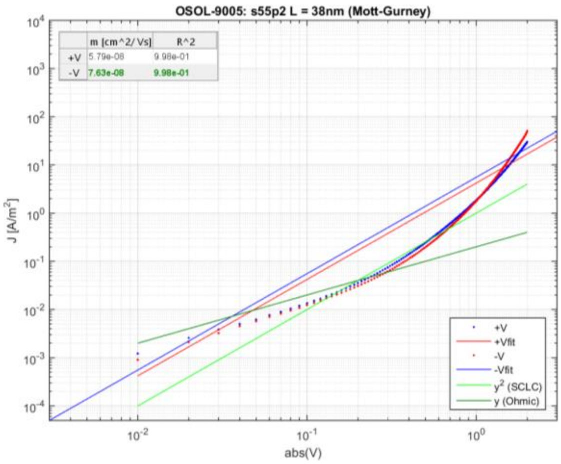

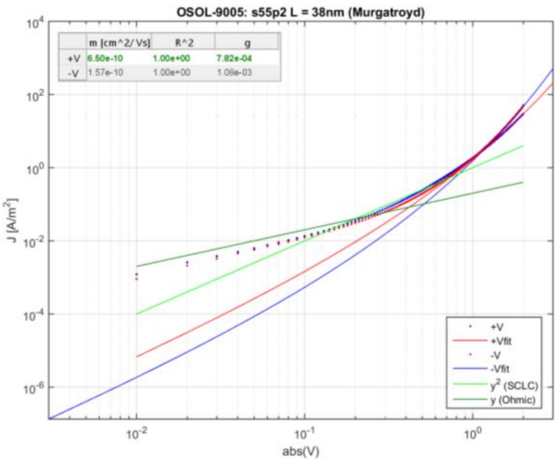

This device also has ohmic contacts, however its mobility field-dependence is higher ($\gamma = 1\cdot10^{-3}\sqrt{cm/V}$), thus the Murgatroyd model is more realistic in its mobility value ($1\cdot10^{-10}$ cm^2/Vs) in comparison with the Mott-Gurney model ($8\cdot10^{-8}$ cm^2/Vs)

Annex G – TPV fit

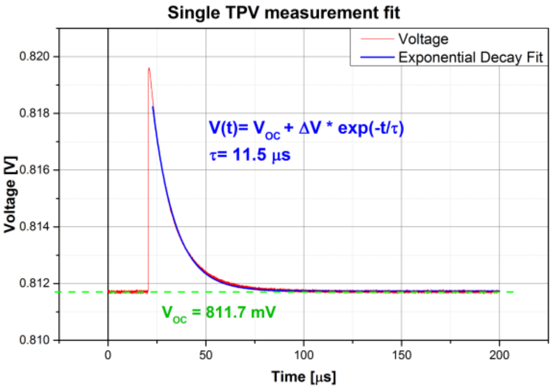

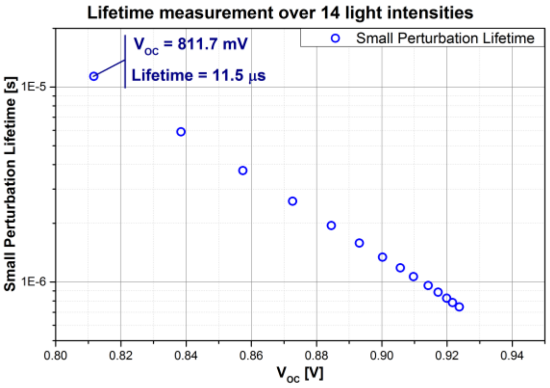

The left side shows a single TPV measurement, which is then fitted according to the exponential decay equation and its lifetime is obtained (11.5 µs). The value for V_{OC} (811.7 mV) is taken from the decay tail as it stabilizes, which ideally should match the plateau located just before the excitation pulse, otherwise errors due to fitting may occur. This procedure is repeated from low to high light intensities and the plot on the right is obtained.

Annex H – n_i fit

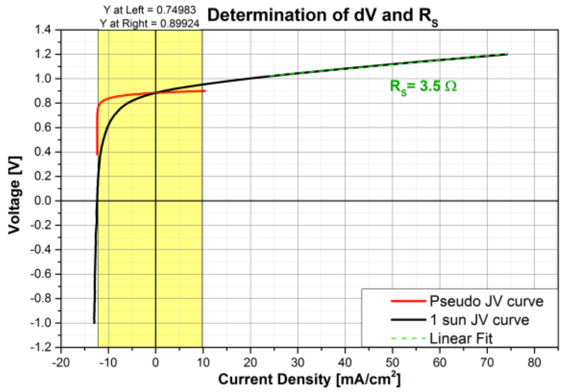

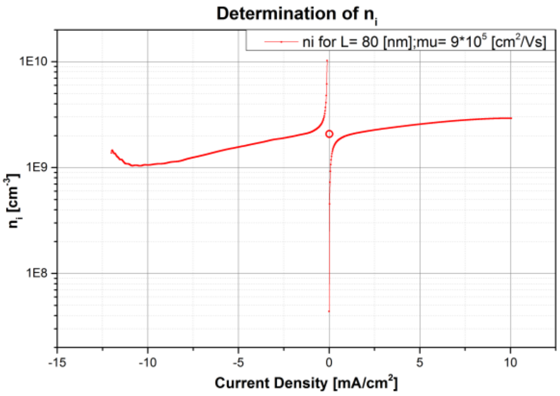

The determination of R_S and the voltage difference (dV) between the pseudo (red) and 1 sun (black) JV curves is located on the left. For this plot the slope directly shows R_S in kΩ (3.5Ω). At the conditions of this fit (high current in forward direction) $R_{tr}(J) \approx 0$, thus $R_S(J) = R_{circ} + R_{tr}(J)$ becomes $R_S(J) = R_{circ}$, where R_{circ} is related to the circuitry of the device. Therefore by knowing R_{circ}, $R_{tr}(J)$ can be calculated. [47]

The voltage differential dV was obtained by interpolation of both plots in the yellow region, as noted on the left, and subtracting them. By applying these parameters to Eq. (1.12), the $n_i(J)$ plot can be obtained as shown on the right. The n_i value at 1sun (thus J=

0) can be determined through extrapolation from the rest of the curve. A pole at this intensity can be observed due to the fact that there is no current flowing. [47]

Annex I – OTRACE

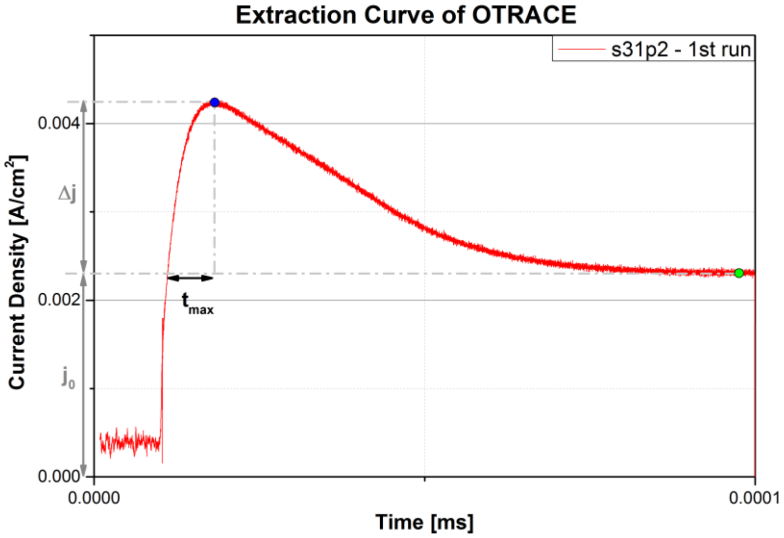

An OTRACE extraction curve at a single delay time is represented above. The maximum and lower level points are determined, respectively in blue and green, as well as the indicated parameters, t_{max}, Δj and j_0. This is repeated for the remaining delay times, where each point in an OTRACE plot corresponds to a delay time. These parameters can then be used with Eq. (1.10) to determine the mobility, as well as other parameters. [42,43]